Structural and metamorphic evolution of the Haimanta Group: Insights from P-T-t-D path modeling of rocks near the Leo Pargil dome, NW India

A Thesis Presented for the
Master of Science
Degree
The University of Tennessee, Knoxville

Kyle Vincent White
December 2014

Acknowledgements

Completion of this project would not have been possible without the generous efforts of numerous faculty members, staff members, and graduate students. I would like to thank the Department of Earth and Planetary Science at the University of Tennessee for five semesters of funding through a Graduate Teaching Assistantship as well as Dr. Micah Jessup for funding through a National Science Foundation research grant.

I would like to thank my advisor, Dr. Micah Jessup, for his help with this project and for making possible a one-month field season in the Indian Himalaya. I would also like to thank my committee members, Dr. Robert Hatcher and Dr. Theodore Labotka, for critical feedback and revisions. It is impossible to overvalue the role Tim Diedesch played in the completion of this project; he offered critical insight into the scientific writing process, served as a field assistant, and performed the geochronologic analyses presented in this paper. I would also like to thank Dr. John Cottle at the University of California, Santa Barbara as well as his lab technicians, who made the geochronologic analyses possible. Allan Patchen also provided extensive assistance with electron microprobe analyses.

Abstract

The metasedimentary rocks of the Haimanta Group in the upper Sutlej Valley, NW India, record an extensive history of Himalayan deformation and metamorphism. Situated beneath the low-grade metasediments of the Tethyan Sedimentary sequence in the hanging wall of the South Tibetan detachment system (STDS), these poly-deformed rocks record Eocene–Oligocene burial metamorphism, crustal thickening and shortening, decompression and mid-crustal melting in the early Miocene, and exhumation along extensional shear zones related to the orogen-parallel exhumation of the Leo Pargil dome (LPD). Low-pressure assemblages (cordierite + sillimanite + quartz) overgrow Barrovian porphyroblasts in Haimanta Group rocks in the NE portion of Sutlej Valley. Detailed petrography on samples collected near the dome indicates a gradient in the intensity of the low-pressure overprint in the Haimanta Group that increases with proximity to the LPD, suggesting that exhumation of this portion of the Haimanta Group was coupled with exhumation of the dome. Quantitative thermobarometry and pressure-temperature-time-deformation (*P-T-t-D*) path modeling suggests that Haimanta Group schists proximal to the LPD record near-isothermal decompression from peak conditions similar to published thermobarometric estimates for the LPD. Combined with previously reported age limits for peak burial, these results indicate that this portion of the Haimanta Group was initially exhumed from mid-crustal depths at a rate similar to the Haimanta Group rocks to the SW that do not show a low-pressure overprint on Barrovian assemblages, although their respective retrograde *P-T* paths show markedly different trajectories. The results indicate that the transition from moderately sloped to steep retrograde *P-T* paths within the Haimanta Group is gradational and does not coincide with a tectonic boundary, and orogen-parallel extension along the Leo Pargil shear zone likely contributed to the differences in the *P-T* histories of these rocks. I present new U-Th-Pb geochronologic results of monazite that place maximum age limits on the development of the crenulation cleavage (S_2) at ~31 Ma and the development of low-pressure overgrowths on Barrovian porphyroblasts at ~27 Ma. The *P-T-t-D* analyses of the Haimanta Group schists may yield implications for orogen-par-

allel dome exhumation and the evolution of the hanging wall rocks of the STDS in this portion of the Himalaya.

Table of Contents

List of Figures

List of Tables

Project overview

The following document is presented as a manuscript that will be submitted to a peer-reviewed journal for publication. My main contributions to this manuscript are: 1) conducting fieldwork (including measuring and recording structural measurements) and sample collection, 2) conducting the electron microprobe analyses for thermobarometric calculations and *in-situ* monazite dating, 3) performing thermobarometric calculations for estimates of peak metamorphic conditions and pseudosection modeling, 4) creating the illustrations, and 5) writing the manuscript.

Purpose of the study

The main objectives of this study are to: 1) characterize the *pressure-temperature-time-deformation* (*P-T-t-D*) evolution of the Haimanta Group rocks near the Leo Pargil dome (LPD) in northwest India, including the relative timing relationships between porphyroblast growth and tectonic fabric development; 2) constrain portions of the *P-T-t-D* paths via *in-situ* U-Th-Pb monazite dating; and 3) characterize the boundary between the rocks of the Haimanta Group and those of the LPD in the northeast portion of Sutlej Valley. Petrographic, geochemical, and geochronologic methods were employed to analyze samples from the Haimanta Group in the central and northeast Sutlej Valley. The resulting data from these analyses permit evaluation of the processes of crustal shortening, burial metamorphism, and exhumation that occurred in this portion of the Himalaya.

Overview of methods

Sample collection took place along a SW-NE transect in the upper Sutlej Valley during the spring of 2013. Samples selected for analysis were chosen from ~29 pelitic schist, leucogranite, and quartz vein material samples collected in 2013 as well as a suite of >200 pelitic schist and leucogranite samples collected by M. Jessup in the summer of 2009. Detailed structural measurements were taken across the transect in order to characterize the history of deformation in the region, a detailed review of which is presented in Jessup et al. (2014, *in review*). Thermobarometric and geochronologic methods were applied to representative samples from each portion of the transect in order to characterize the *P-T-t-d* of the Haimanta Group, especially with respect to exhumation of the LPD. Details of these methods are included within each chapter.

P-T estimates

Representative samples from the garnet- and staurolite-kyanite-grade rocks in the Haimanta Group were selected for thermobarometric analyses. Petrographic analyses of these samples were used to evaluate the relationship between phases such as garnet, staurolite, plagioclase, biotite, and muscovite that were factored into the *P-T* calculation. Mineral compositions were measured on a Cameca SX-100 electron microprobe (EMP) housed at the University of Tennessee. X-ray compositional maps of garnet porphyroblasts were conducted to determine zonation patterns of Mg, Fe, Ca, and Mn and were combined with quantitative point transects across each grain to interpret the conditions associated with garnet growth. Compositional analyses were also conducted for other phases such as staurolite, plagioclase, biotite, and muscovite to determine the presence of any compositional heterogeneities among grains across the thin section. *P-T* estimates for peak metamorphic conditions were calculated from the compositional data using the THERMOCALC 3.33 thermobarometric software (Powell & Holland, 1998) in the average *P-T* mode. Activity coefficients for each phase were calculated using the AX software. The results of these calculations yield estimates of *P-T* conditions at peak metamorphic temperatures.

In order to fully characterize the burial and exhumation histories of the staurolite-kyanite-grade rocks in the central and NE portions of Sutlej Valley, *P-T* paths were constructed for these rocks using pseudosection modeling. This method requires calculation of the bulk composition of a sample, which was performed by combining compositional data from each phase with a point counting modal analysis across the entire thin section. The results of these calculations predict the mineral assemblages that should be stable at particular *P-T* conditions. Petrographic evidence of the assemblages in equilibrium and the reactions recorded in the sample allow for the interpretation of a *P-T* path undergone by the sample. The Perplex 6.6.8 software package (Connolly, 2009; updated in 2011) was used for pseudosection calculation using the Holland and Powell (1998) thermodynamic dataset (updated in 2004, *hp04ver.dat*). The Perplex software also allows for the modeling of the change in chemical composition of a particular phase (e.g. Mn content in garnet) as well as the change in modal percentage of a particular phase throughout *P-T* space for a given bulk composition. These results are often contoured and overlain on a pseudosection and can be combined with compositional data obtained on the EMP and petrographic analyses to assist in *P-T* path interpretation. For clarity, the results of these methods in this study have been plotted using a simple Matlab script available for download on the Perplex website.

In-situ monazite geochronology

U-Th-Pb monazite geochronologic methods were applied to the samples that were selected for psuedosection calculation to place timing constraints on portions of the interpreted *P-T* paths for these rocks. Integrating these data with the *P-T* estimates places limits on the timing of prograde metamorphism and the onset of decompression. U-Th-Pb geochronology involves the radioactive decay of ^{238}U, ^{235}U, and ^{232}Th to ^{206}Pb, ^{207}Pb, and ^{208}Pb, respectively. This method is ideal for minerals that contain an abundance of these isotopes such as monazite, which incorporates large amounts of U and Th, has high retentivity of Pb, and has a relatively high closure temperature (e.g. Parrish, 1990; Kohn & Malloy, 2004). The ratios of these isotopes were used to calculate the age at which monazite crystallized in these samples based on the following equations (Jaffey, et al., 1971; Dicken, 2005):

$$(^{206}Pb / ^{238}U) = e^{\lambda 238\, t} - 1 \quad (1)$$

$$(^{207}Pb / ^{235}U) = e^{\lambda 235\, t} - 1 \quad (2)$$

$$(^{208}Pb / ^{232}Th) = e^{\lambda 232\, t} - 1 \quad (3)$$

where λ is a decay constant and t is the half-life of decay, assuming a closed system. Potential causes of discordance are Pb loss during heating, the presence of common Pb, and/or age domain mixing during acquisition of the analyses.

U-Th-Pb analyses from the staurolite-kyanite-grade samples used for pseudosection calculation provides estimates of the timing of monazite crystallization during metamorphism. Performing the analyses *in-situ* allows for relating monazite growth to metamorphic reactions that occurred in the sample as well as the growth of phases such as garnet, which was used for *P-T* estimate calculation. In metapelitic rocks at amphibolite-grade conditions, Y content in monazite has been shown to be controlled by garnet in the absence of xenotime and by xenotime in the absence of garnet (e.g. Spear & Pyle, 2010), as garnet sequesters the majority of Y during growth. Relatively high-Y domains in monazite grains may therefore be related to garnet breakdown reactions (e.g. Foster et al., 2002). *In-situ* monazite analysis also permits placing limits on the timing of fabric development in these samples. U-Th-Pb analyses of monazite grains were conducted on the laser ablation inductively coupled mass spectrometer (LA-ICPMS) at the University of California, Santa Barbara.

Chapter 1: Introduction

Records of crustal-scale processes often manifest in grain-scale features in metamorphic rocks. These features include, among others: inclusion trail geometries in poikiloblastic minerals (e.g. Vernon, 1978; Bell & Rubenach, 1982; Williams, 1994), chemical zonation in porphyroblasts (e.g. Spear et al., 1984; Ganguly et al., 2000; Caddick et al., 2010), and reaction textures around metamorphic minerals (e.g. Gieré et al., 2011; White & Powell, 2011). Medium- to high-grade pelitic schist is especially useful in this regard because they frequently contain many of these features as well as a record of the mechanical processes (e.g. tectonic foliation formation, shearing) that may accompany metamorphism (e.g. Simpson & Schmid, 1983). The formation of regional metamorphic terranes often coincides with progressive deformation, as the burial of rocks to the depths required for metamorphism involves mass movement on a crustal scale (e.g. England & Thompson, 1984). The Himalaya offer the opportunity to study the relationships between deformation and metamorphism in an active orogenic setting, and near-perfect exposure of the metamorphic core of the orogen makes it an ideal locale to study mountain-building processes and the evolution of metamorphism during orogeny.

The Himalayan orogen is the focus of numerous studies investigating the metamorphic and mechanical responses to burial and exhumation during orogeny (e.g. Windley, 1983; Searle et al., 1987; Vannay & Grasemann, 2001; Beaumont et al., 2001), and these studies have provided a framework for the creation of tectonic reconstruction models for the Himalaya (e.g. Nelson et al, 1996; Beaumont et al., 2001; Grujic et al., 1996, 2002; Vannay et al., 2004). Of particular interest to earth scientists has been the evolution of the metamorphic core of the Himalaya, the Greater Himalayan Sequence (GHS), which occurs in the hanging wall of the Main Central thrust (MCT) and below the normal faults of the South Tibetan detachment system (STDS). Pressure-temperature (*P-T*) and geochronologic studies of the unit support the interpretation that the MCT and STDS were simultaneously active during the Miocene (e.g. Hodges et al., 1992; Dèzes et al., 1999; Godin et al., 2001), which led to the tectonic exhumation of the GHS. From these results, numerous models for the extrusion of the GHS have been proposed, including south-directed ductile flow (i.e. “channel flow”; Beaumont et al., 2001; Godin et al., 2006) and extrusion as an orogenic wedge (dubbed “general shear extrusion” by Vannay & Grasemann, 2001). The deformed gneisses of the GHS also occur in the hinterland of the orogen as a series of isolated domes collectively known as the North Himalayan gneiss domes (e.g. Burg et al., 1994; Chen et al., 1990; Lee et al., 2004; Larson et al., 2010). *P-T* and thermochronologic analyses on the GHS gneisses and the overlying schists of the Tethyan Sedimentary sequence (TSS) (e.g. Lee et al., 2000; Quigley et al., 2006) have led to numerous hypotheses for the exhumation of these domes. For example, the Kangmar dome in southern Tibet is proposed to have formed via purely contractional mechanisms (Burg et al., 1984), orogen-perpendicular extensional mechanisms a lá the metamorphic core complexes of the North American Cordillera (Chen et al., 1990), or a combination of the two (Lee et al., 2000).

Conversely, recent studies have shown the importance of orogen-parallel extension in the evolution of the Himalaya and the unroofing of mid-crustal rocks (e.g. Coleman, 1996; Xu et al., 2013). The Leo Pargil dome (LPD), located in NW India, differs from the North Himalayan gneiss domes in that it was exhumed by orogen-perpendicular normal faults (Thiede et al., 2006), similar to the nearby Gurla Mandhata core complex (Murphy et al., 2002) and the Ama Drime Massif (Jessup et al., 2008; Jessup & Cottle, 2010; Cottle et al., 2009). Although interpretations for the mechanisms for exhumation of the LPD differ, the Karakorum fault is believed to be responsible for the regional stress field that favors orogen-parallel extension (e.g. Thiede et al., 2006; Hintersberger et al., 2010, 2011; Langille et al., 2014). The dome consists of a core of migmatite and leucogranite bound by amphibolite-grade gneiss that is intruded by several generations of leucogranite dikes and sills (Langille et al., 2012). The LPD is bound on the west by the Leo Pargil shear zone (LPSZ), a west-dipping zone with a dominant WNW-plunging mineral stretching lineation that indicates top-down-to-the-west displacement (Thiede et al., 2006; Langille, et al., 2012). The LPSZ juxtaposes the mid-crustal gneisses of the LPD against the overlying metasedimentary rocks of the TSS and the Haimanta Group (Langille et al., 2012). The amphibolite-grade schists of the Haimanta Group are separated from the LPD along the southern flank by a ~5-km-wide zone of leucogranite dikes and sills (Fig. 1).

Previous work on the LPD and the Haimanta Group schists consists of the low-temperature (< 350°C) exhumation history of the rocks in the footwall of the LPSZ (Thiede et al., 2006), timing of mid-crustal partial melting and leucogranite crystallization (Leech, 2008; Lederer et al., 2013), and *P-T-t-D* (pressure-temperature-time-deformation) path calculations for the rocks of the LPD (Langille et al., 2012) and the Haimanta Group away from the LPD (Chambers et al., 2009; Jessup et al., *in review*). Although much of the metamorphic and structural history of the LPD rocks has been deciphered, there is much to gain by studying the evolution of the Haimanta Group. As such, this study attempts to fill in significant gaps in the *P-T-t-d* constraints for the Haimanta Group schist adjacent to the LPD. The metasedimentary rocks of the Haimanta Group record burial to regional metamorphic depths as well as retrograde metamorphic reactions and textures associated with emplacement of the LPD (Chambers et al., 2009; Langille et al., 2012). Characterizing the relationship between the Haimanta Group and the LPD as well as quantifying the *P-T-t-d* history of the rocks adjacent to the LPD permit the opportunity to document the differences in *P-T* histories between the crenulated schist of the Haimanta Group and the rocks with the Miocene overprint on Barrovian metamorphism.

Geologic background

The 2500-km-long Himalayan front represents the highest mountain chain in the world, extending from the Indus River, Nanga Parbat in the NW to the Brahmaputra River, Namche Barwa in the E (e.g. Gansser, 1980; Le Fort, 1975). North-directed collision of the Indian Plate with the Asian Plate began in the late Cenozoic—estimates range from as late as > 62 Ma (e.g. Hu et al., 2012) to later than ~35 Ma (e.g. Najman et al., 2010)—and the orogeny has accommodated a significant amount of crustal shortening and thickening since. Early (Eocene to middle Miocene) shortening was accommodated by the Main Central thrust (MCT), while more recent deformation is restricted to thrust faults associated with the Main Boundary thrust towards the foreland (Figure 1a). The Himalaya is divided into three lithotectonic units separated by major fault systems (in order of increasing structural level): metasedimentary rocks of the Lesser Himalayan Series (LHS), metamorphic and igneous rocks of the Greater Himalayan Series (GHS), and the Tethyan Sedimentary Sequence (TSS), which consists of Upper Proterozoic to Eocene passive Indian margin sediments with metamorphic grade ranging from unmetamorphosed to amphibolite grade (Vannay et al., 2004). The LHS is bound at the bottom by the MBT and at the top by the MCT, which juxtaposed the GHS on the LHS. The GHS is bound at the top by the low-angle, normal displacement South Tibetan detachment system (STDS), which juxtaposes TSS in the hanging wall on GHS in the footwall (Vannay and Grasemann, 2001; Vannay et al., 2004). Movement along the STDS accommodated top-to-the-NE displacement and extrusion of the metamorphic core of the Himalaya during the Miocene (e.g. Grujic et al., 1996, 2002; Searle & Godin, 2003) as late as 10–12 Ma (e.g. Edwards & Harrison, 1997).

In the central Himalaya, movement along the STDS was cross cut by shear zones and faults that accommodated orogen-parallel extension and are kinematically linked with faults in the Tibetan interior (e.g. Jessup et al, 2008; Jessup & Cottle, 2010). This E-W extension caused the uplift of features that dissect the southern edge of the Tibetan Plateau (e.g. the Ama Drime Massif) (Langille et al., 2010). The Gurla Mandhata core complex and the LPD, in the western Himalaya, record orogen-parallel extension along NE-SW-oriented shear zones and faults (e.g. the Gurla Mandhata detachment and the LPSZ) that are kinematically linked to dextral displacement along the Karakorum fault (e.g. Thiede et al, 2006; Saylor et al., 2010; Murphy et al., 2002, 2009). The LPD is bound on the east by the Qusum detachment (Zhang et al., 2000), which marks the western boundary of the Zhada basin (e.g. Saylor et al., 2010).

Geology of the upper Sutlej Valley

The Sutlej River in NW India, Himachal Pradesh, runs roughly NE-SW and exposes the three lithotectonic units that comprise the Himalaya. In the southern end of the valley, the migmatitic gneisses of the GHS occur above the low-grade metasedimentary rocks of the LHS with the two units separated by mylonites of the MCT (Vannay & Grasemann, 2001). Detailed structural and thermobarometric analysis of the GHS in the Sutlej Valley (Vannay & Grasemann, 2001) reveals that the unit features a pervasive NE-dipping foliation and an inverted metamorphic temperature gradient with staurolite-grade rocks at the base and migmatite-grade rocks at the uppermost structural levels. The GHS is bound at the top by a thick section of mylonites associated with top-down-to-the-north movement along the Sangla detachment, the local equivalent of the STDS. Above the Sangla detachment, the Akpa granite occurs as an intrusion along the base of the Haimanta Group (Frank et al., 1995), the local equivalent of the Everest Series (e.g. Searle et al., 2003) and the Upper Bhimpedi Group in the Kathmandu Nappe (e.g. Yin, 2006), among others.

The Haimanta Group in Sutlej Valley consists of interlayered meta-pelites and -psammites, much of which has undergone amphibolite-grade metamorphism (Chambers et al., 2009). At the base near the Akpa granite, the unit features a penetrative, moderately NE-dipping foliation (S_2, a crenulation cleavage), NE-plunging mineral stretching lineations, and folds featuring consistently NW-SE-striking axial surfaces (Vannay & Grasemann, 2001). The rest of the Haimanta Group section in Sutlej Valley was previously interpreted by Chambers et al. (2009) as a meso-scale, broad synform with a NE-dipping axial surface; however, detailed structural analysis by Jessup et al. (*in review*) suggests that the structure in the Haimanta Group consists of a

Figure 1: Regional geologic map and cross section. (A) Digital elevation map (from SRTM) of the western Himalaya modified from Lederer et al. (2013) and Langille et al. (2012). White area indicates location of geologic map; (B) Simplified geologic map of the upper Sutlej Valley modified from Jessup et al. (*in review*). Orange unit in NE portion of map area represents the paragneiss and leucogranite of the Leo Pargil dome (LPD). A to A' line denotes cross section location. Yellow dashed lines are metamorphic isograds; (C) Cross section from A to A'. Colors correspond to those in (B).

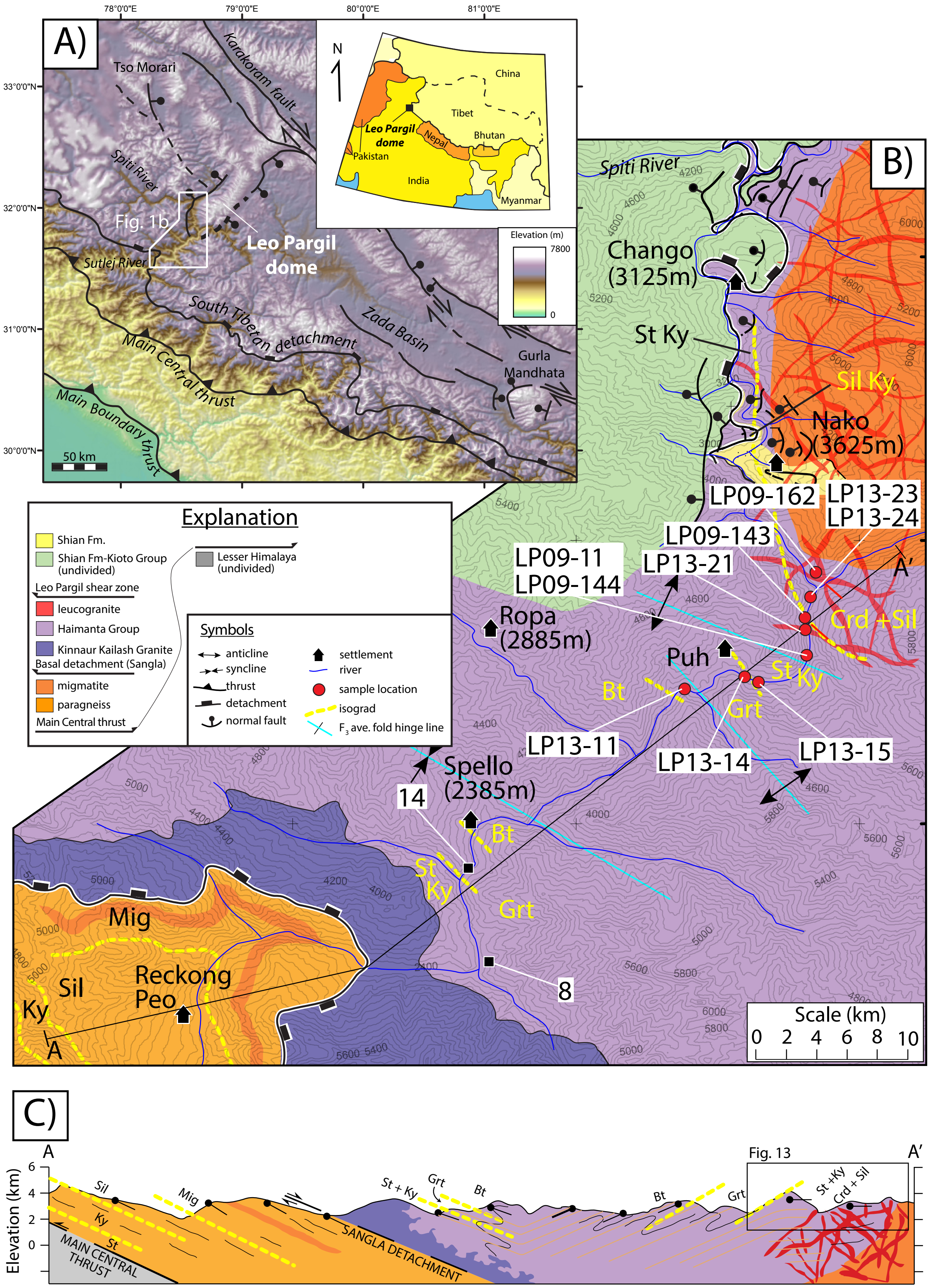
A)
Tso Morari
Karakoram fault
Spiti River
Fig. 1b
Leo Pargil dome
Sutlej River
South Tibetan detachment
Zada Basin
Main Central thrust
Main Boundary thrust
Gurla Mandhata
50 km
China
Tibet
Leo Pargil dome
Nepal
Bhutan
Pakistan
India
Myanmar
Elevation (m)
B)
Spiti River
Chango (3125m)
St Ky
Sil Ky
Nako (3625m)
LP09-162
LP13-23
LP13-24
LP09-143
LP09-11
LP09-144
LP13-21
Crd +Sil
Ropa (2885m)
Puh
St Ky
Bt
Grt
LP13-11
LP13-14
LP13-15
Spello (2385m)
14
Bt
St Ky
Grt
8
Mig
Sil
Ky
Reckong Peo
Scale (km)
Explanation
Shian Fm.
Shian Fm-Kioto Group (undivided)
Leo Pargil shear zone
leucogranite
Haimanta Group
Kinnaur Kailash Granite
Basal detachment (Sangla)
migmatite
paragneiss
Main Central thrust
Lesser Himalaya (undivided)
Symbols
anticline
syncline
thrust
detachment
normal fault
settlement
river
sample location
isograd
F3 ave. fold hinge line
C)
Elevation (km)
Fig. 13
Sil
Ky
St
Mig
MAIN CENTRAL THRUST
SANGLA DETACHMENT
St + Ky
Grt
Bt
St +Ky
Crd + Sil

Figure 1.

more complicated poly-deformational history with higher-frequency F_3 folds deforming the dominant S_2 fabric. For a detailed structural review, see Jessup et al. (*in review*). The contact between the Haimanta Group and the overlying low-grade, Ordovician to Jurassic metasedimentary rocks of the TSS has been interpreted as an unconformity (Wiesmayr & Grasemann, 2002).

The pelitic schists of the Haimanta Group record Barrovian metamorphism beginning in the Eocene (e.g. Chambers et al., 2009). The kyanite-grade rocks at the base of the section near the Akpa granite were interpreted by Chambers et al. (2009) to have experienced peak metamorphic conditions of 640–660°C and 6–7 kbar. U-Pb monazite ages limit garnet growth between >34 and 28 Ma, with maximum burial achieved by ~30 Ma (Chambers et al., 2009). From the base, metamorphic grade decreases to the northeast, with biotite-grade rocks representing the highest structural levels in the Haimanta Group near the village of Spello (Fig. 1). From the biotite zone to the northeast, metamorphic grade increases through the garnet-in and staurolite- and kyanite-in isograds to sillimanite-grade rocks at the confluence of the Sutlej and Spiti Rivers, near the LPD (Jessup et al., *in review*). The sillimanite-grade rocks in the NE portion of the Sutlej Valley are intruded by a swarm of cm- to m-scale leucogranite dikes and sills (Fig. 1) (e.g. Langille et al., 2012; Lederer et al., 2013). The leucogranites are derived from partial melting at mid-crustal depths and yield U-Pb monazite crystallization ages ranging from 30 to 18 Ma (Lederer et al., 2013).

Decompression

In the NE portion of the Sutlej Valley, Barrovian porphyroblasts are consistently overprinted by relatively lower-pressure assemblages with increasing intensity with proximity to the LPD, in contrast to the Haimanta Group rocks to the SW, which feature little evidence of retrograde metamorphism. Samples LP09-144, LP13-21, LP09-143, LP13-23, and LP13-24 (listed from SW to NE) exhibit a low-pressure overprint on Barrovian porphyroblasts (Fig. 2).

Sample LP09-144 (31.7586 °N, 78.6311 °E) (Figs. 2a & 2b), collected east of the village of Pooh (Fig. 1), is a staurolite-kyanite schist comprised of an anastomosing S_2 foliation that warps around staurolite and kyanite porphyroblasts. Staurolite and kyanite occur as intergrowths and isolated grains and feature linear and sigmoidal inclusion trails at an angle to the matrix foliation, which is defined by interlayered mica and quartz domains. Staurolite and kyanite grains are consistently overprinted by quartz and pinite, a common retrograde product of cordierite breakdown reactions (e.g. Lal, 1969) (Figs. 2a & 2b). Most of the biotite in the sample is re-placed by chlorite. The sample also contains minor amounts of muscovite, tourmaline, rutile, and zircon.

Sample LP13-21 (31.7837 °N, 78.6370 °E) (Figs. 2c & 2d), collected ~2 km north of LP09- 144 (Fig. 1), is a kyanite schist with kyanite porphyroblasts occurring with long axes subparallelto an anastomosing S_2 foliation defined by quartz, biotite, and chlorite. Kyanite grains are resorbed along their rims by cordierite and pinite (Figs. 2c & 2d). Cordierite is a common low-pressure breakdown product of staurolite and kyanite (e.g. Brown & Earle, 1983). Much of the biotite in this sample has been consumed by chlorite, and the rest of the sample consists of quartz, feldspar, and muscovite with minor amounts of apatite and rutile.

Sample LP09-143 (31.7835 °N, 78.6365 °E) (Figs. 2e & 2f), collected ~300 m north of LP13-21 (Fig. 1), is a staurolite schist with large (sub-cm-scale) staurolite porphyroblasts with linear inclusion trails that are roughly continuous with the matrix foliation comprised of quartz, feldspar, and mats of biotite. As this sample was unoriented when collected, it is difficult to make interpretations regarding relative timing of staurolite growth with respect to foliation develop-ment. Staurolite grains are consistently overgrown by cordierite, only a minor amount of which has broken down to pinite (Figs. 2e & 2f). The biotite in this sample is intact and has not under-gone breakdown to chlorite. This sample also contains minor amounts of muscovite, ilmenite, and rutile.

Figure 2: Representative photomicrographs and field photo of Haimanta Group samples in the NE portion of Sutlej Valley. Note that, from top to bottom, locations of photos move progressively northeast towards the Leo Pargil dome, and the extent of the low-pressure overprint on Barrovian porphyroblasts increases from sample LP09-144 to the northeast. (A) & (B): Kyanite porphyroblast from sample LP09-144 showing overgrowth of quartz and pinite along rim in plane-polarized (A) and cross-polarized (B) light; (C) & (D): Kyanite porphyroblast from sample LP13-21 showing cordierite and pinite overgrowths along rim in plane-polarized (C) and cross-polarized (D) light; (E) & (F): Staurolite porphyroblast in sample LP09-143 with cordierite and pinite overgrowths along rim in plane-polarized (E) and cross-polarized (F) light; (G): Field photo from outcrop where sample LP13-23 was taken. View is vertical down on S_1 plane showing staurolite porphyroblast (or possible remnants thereof) intergrown with tourmaline with cordierite overgrowth along rim. Schematic diagram illustrates this relationship; (H): Plane-polarized light photomicrograph of sample LP13-23 showing cordierite and tourmaline "aggregates" (see text), possibly remnants of Barrovian porphyroblasts; (I): Plane-polarized light photomicrograph of resorbed kyanite porphyroblasts consumed by a quartz- and cordierite-forming reaction in sample LP13-24; (J) Plane-polarized light photomicrograph of resorbed kyanite porphyroblast consumed by quartz-, cordierite-, and sillimanite-forming reactions in sample LP13-24, near the Leo Pargil dome.

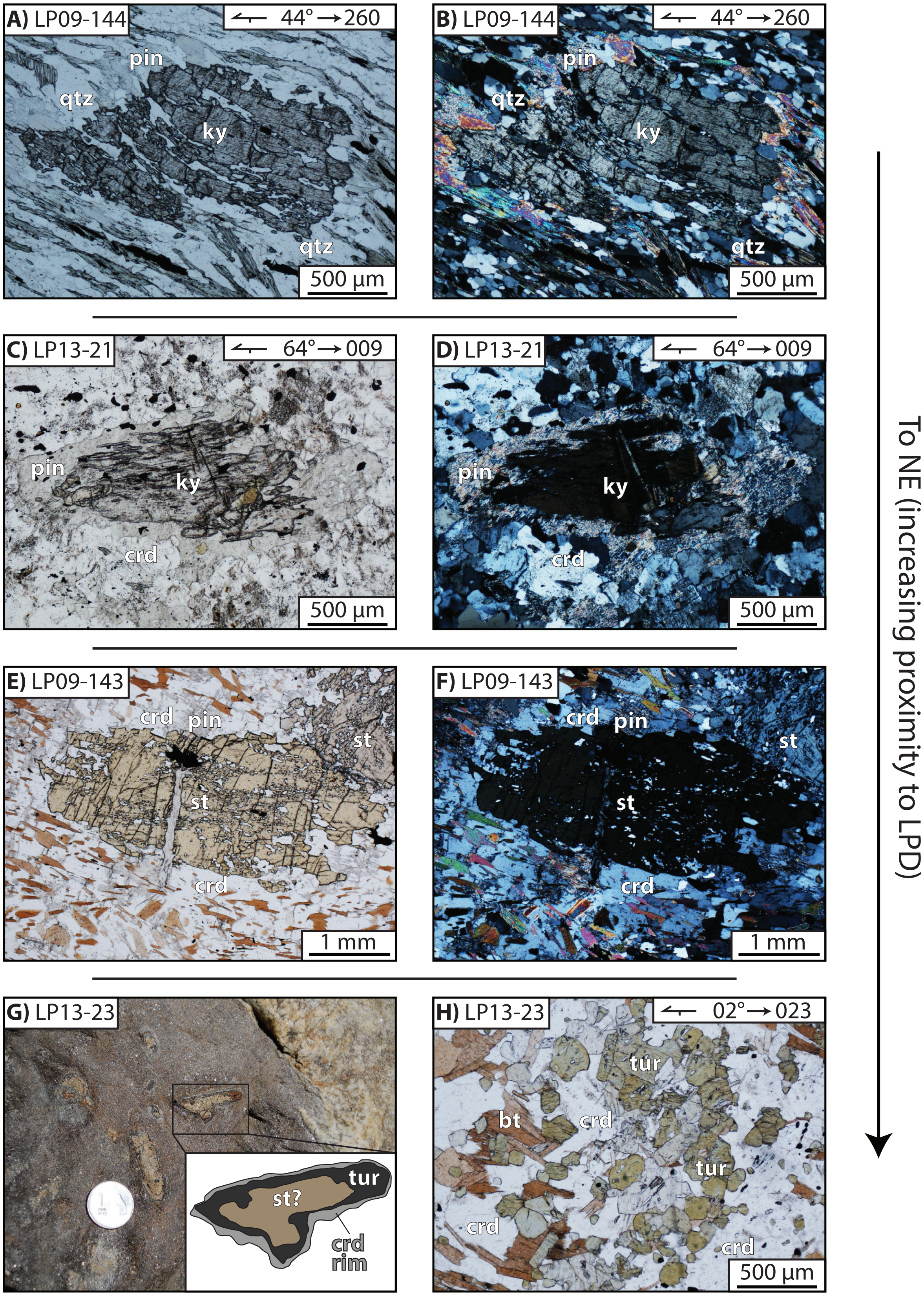
A) LP09-144
44° → 260
pin
qtz
ky
qtz
500 µm
B) LP09-144
44° → 260
pin
qtz
ky
qtz
500 µm
C) LP13-21
64° → 009
pin
ky
crd
500 µm
D) LP13-21
64° → 009
pin
ky
crd
500 µm
E) LP09-143
crd
pin
st
st
crd
1 mm
F) LP09-143
crd
pin
st
st
crd
1 mm
G) LP13-23
tur
st?
crd
rim
H) LP13-23
02° → 023
tur
bt
crd
tur
crd
crd
500 µm
To NE (increasing proximity to LPD)

Figure 2.

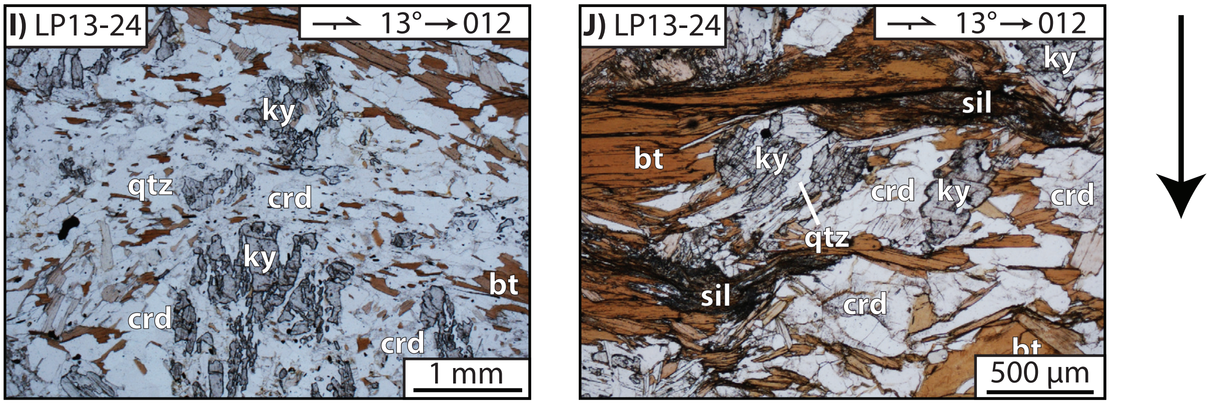

Figure 2 (*continued*).

Sample LP13-23 (31.7963 °N, 78.6386 °E) (Figs. 2g & 2h), collected ~300 m south of theconfluence of the Sutlej and Spiti Rivers (Fig. 1), is a tourmaline-cordierite schist consisting of aggregates of intergrown tourmaline and cordierite in a foliated matrix of biotite, quartz, and feldspar. Originally identified as staurolite with a cordierite-sillimanite reaction rim when collected in the field (Fig. 2g), the aggregates of tourmaline and cordierite in this sample are interpreted as cordierite growth from a pelitic assemblage of staurolite and/or kyanite, all of which has reacted out. This sample also contains minor amounts of sillimanite, muscovite, and ilmenite.

Sample LP13-24 (31.7965 °N, 78.6371 °E) (Figs. 2i & 2j), collected within ~50 m of LP13-23, is a kyanite-cordierite schist with kyanite porphyroblasts featuring sigmoidal inclusion trails in a foliated matrix defined by quartz, feldspar, and mats of biotite. Kyanite is metastable and shows evidence for breakdown to cordierite. Cordierite occurs as both a breakdown product along kyanite rims (Fig. 2i) and as isolated porphyroblasts. This sample also contains minor amounts of muscovite, rutile, and zircon.

Chapter 2: Thermobarometry

Samples

Four samples that best represent the *P-T-t-D* history of Haimanta Group rocks were chosen for thermobarometric and geochronologic analyses from two suites of samples: 1) 29 pelitic schist, leucogranite, and quartz vein material samples collected in 2013; and 2) >200 pelitic schist and leucogranite samples collected by M. Jessup in 2009. Three pelitic samples (LP13-11, LP13-14, and LP13-15) from the 2013 suite collected near the village of Pooh were chosen because they feature Barrovian porphyroblasts that record the *P-T-t-D* history of the Haimanta Group without any overprinting associated with emplacement of the LPD. One pelitic sample (LP09-11) from the 2009 suite collected to the NE of Pooh was selected because it features Barrovian porphyroblasts that are partially overprinted by relatively lower-pressure assemblages associated with top-down-to-the-west shearing and decompression related to emplacement of the LPD.

Sample LP13-11 (31.7464° N, 78.5745° E) is a pelitic schist that was collected within the garnet zone rocks south of the village of Pooh (Fig. 1). Euhedral garnet porphyroblasts preserve a relict fabric in the form of linear inclusion trails (S_1) and occur in a foliated matrix defined by mats of biotite and muscovite and domains of quartz and albite (S_2) (Fig. 3a). Chlorite is rare but occurs as a retrograde breakdown product of biotite and along C' bands that offset the dominant S_2 matrix foliation. Garnet porphyroblasts are fractured and contain inclusions of quartz, albite, apatite, and ilmenite. Accessory ilmenite, apatite, and zircon occur throughout the matrix. Quartz exhibits undulose extinction and sub-grains. Minor amounts of kyanite occur in the matrix, but textural analysis and P-T estimates (see *P-T Estimates* section) support the interpretation that this sample is from the garnet zone.

Sample LP13-14 (31.7570° N, 78.5977° E) is a pelitic schist comprised of euhedral stau-

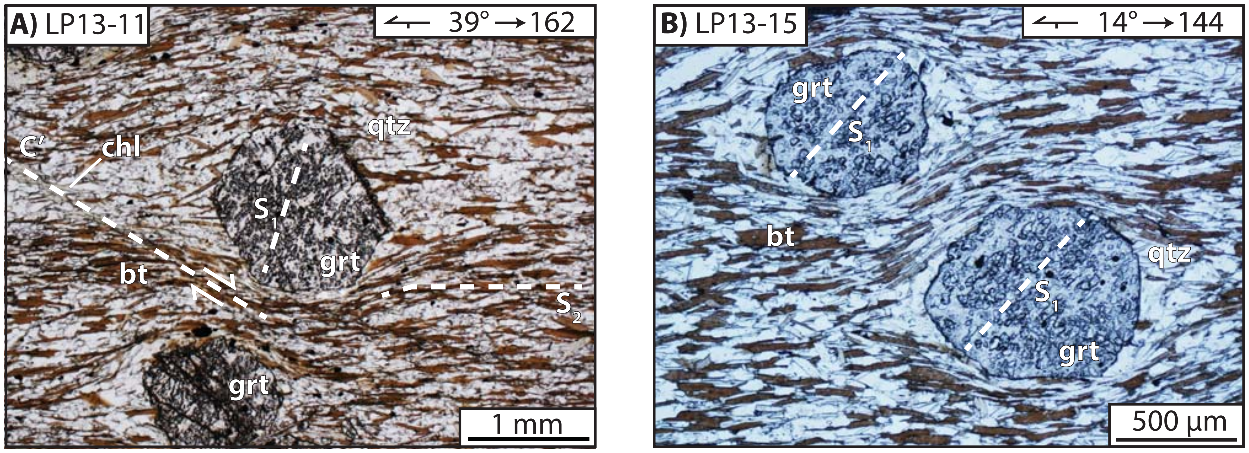

Figure 3: Plane-polarized light photomicrographs of garnet-zone samples. (A) Garnet porphyroblasts in sample LP13-11 show overgrowth of an early fabric, S_1, in a foliated matrix; (B) Garnet porphyroblasts in sample LP13-15 show a similar overgrowth to (A).

rolite and kyanite porphyroblasts that was collected in the transition zone between garnet- and staurolite-kyanite-grade rocks east of Pooh (Fig. 1). The dominant matrix foliation consists of a crenulation cleavage (S_2) defined by interlayered mats of muscovite and biotite (Fig 4a). Inclusion trail geometry supports the interpretation that kyanite—and, to a lesser extent, staurolite—overgrows the crenulation cleavage, S_2 (Fig. 4b). Crenulation limbs (S_1) are comprised of interlayered biotite, muscovite, and chlorite as well as domains of albite and quartz. Individual biotite grains also occur at high angles to the matrix foliation. Kyanite and staurolite contain inclusions of quartz, albite, muscovite, ilmenite, monazite, and apatite. Garnet is rare but is occluded by kyanite and is partially replaced by chlorite (Fig. 4c). Accessory amounts of ilmenite, rutile, zircon, monazite and xenotime occur throughout the matrix. Quartz exhibits undulose extinction, sub-grains, and lobate grain boundaries.

Sample LP13-15 (31.7557° N, 78.6006° E) is a pelitic schist that was collected ~200 m east of LP13-14 (Fig. 1) in the transition zone between garnet- and kyanite-grade rocks. Euhedral garnet porphyroblasts occur in a matrix defined by interlayered biotite and muscovite and domains of quartz and albite (S_2; 234°, 14° SE) and preserve a relict fabric (S_1) in the form of

Figure 4: Plane-polarized light photomicrographs of staurolite-kyanite grade samples. (A) Mosaic of sample LP13-14 showing dominant crenulation cleavage (S_2) fabric. Staurolite overgrows a partially-developed S_2; (B) Kyanite overgrowth of a fully developed S_2 fabric in sample LP13-14; (C) Garnet occluded by kyanite and subsequently resorbed by chlorite in sample LP13-14; (D) Staurolite with sigmoidal inclusion trails suggesting syntectonic top-down-to-the-west growth in sample LP09-11; (E) Pinite overgrowths on staurolite in sample LP09-11.

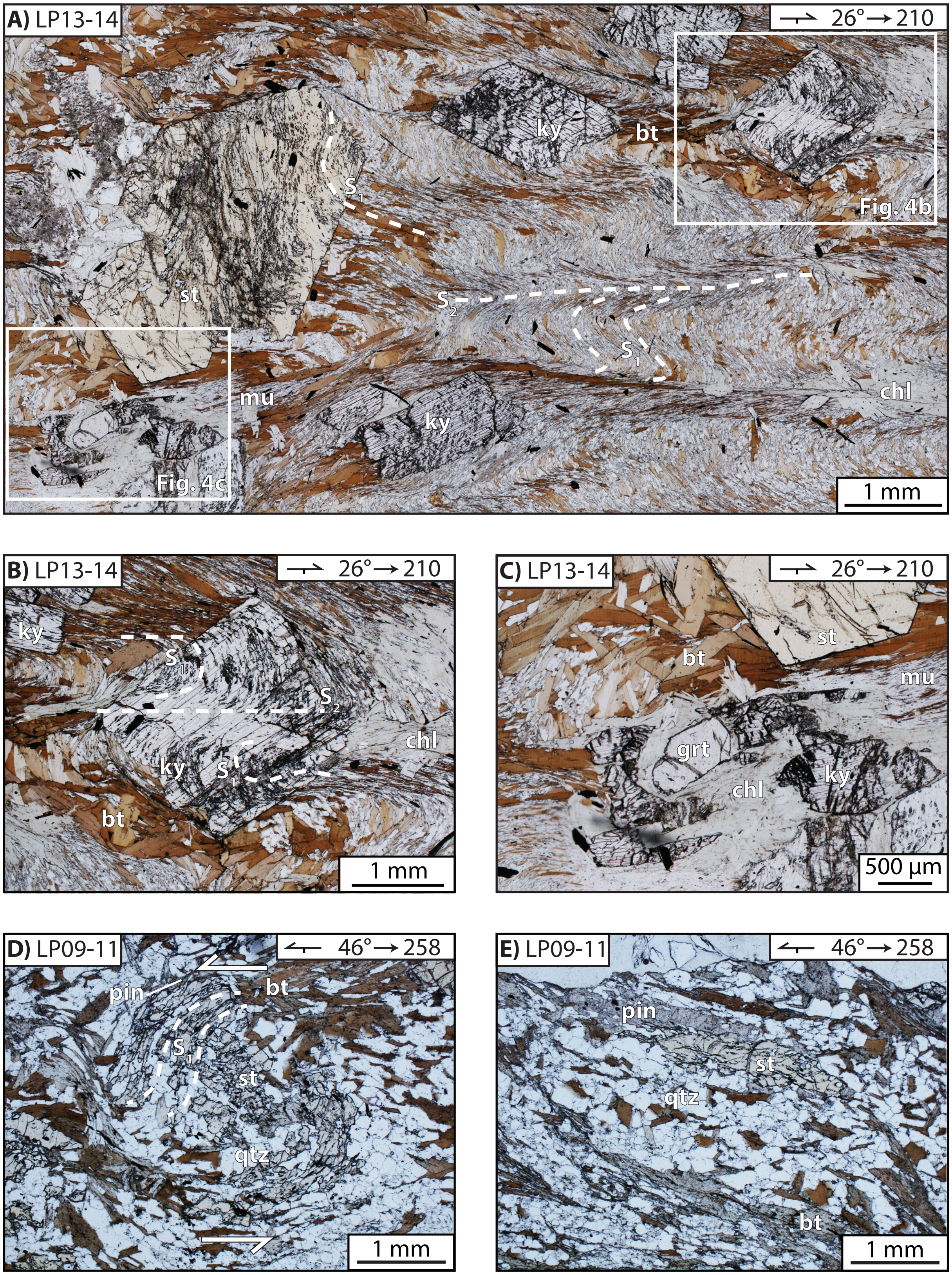

A) LP13-14
26° → 210
ky
bt
st
S1
S2
S1
Fig. 4b
mu
ky
chl
Fig. 4c
1 mm
B) LP13-14
26° → 210
ky
S1
S2
chl
ky
S1
bt
1 mm
C) LP13-14
26° → 210
st
bt
mu
grt
chl
ky
500 µm
D) LP09-11
46° → 258
pin
bt
S1
st
qtz
1 mm
E) LP09-11
46° → 258
pin
st
qtz
bt
1 mm

Figure 4.

inclusion trails (Fig. 3b). Inclusions in garnet consist of quartz, albite, ilmenite, and apatite. Pressure shadows comprised of quartz, albite, and biotite occur around garnet porphyroblasts. Minor amounts of ilmenite, rutile, and zircon occur throughout the matrix. Chlorite occurs mainly as a breakdown product of biotite. Quartz exhibits undulose extinction and lobate grain boundaries.

Sample LP09-11 (31.7606° N, 78.6358° E) was collected in the staurolite-kyanite zone NE of Pooh near the LPD (Fig. 1). This sample is a pelitic schist comprised of staurolite and kyanite porphyroblasts in a foliated matrix of biotite, muscovite, quartz, and plagioclase (S_2; 168°, 46° SE). Kyanite occurs as both an intergrowth with staurolite and as an inclusion in staurolite. Staurolite porphyroblasts contain sigmoidal inclusion trails of quartz, biotite, apatite, and monazite (Fig.4d). Small amounts of chlorite, ilmenite, and rutile also occur throughout the matrix. Staurolite and kyanite are partially overgrown by quartz, albite, cordierite, and pinite (a common retrograde alteration product of cordierite breakdown; Lal, 1969) (Fig. 4e). Quartz exhibits undulose extinction and lobate grain boundaries.

Methodology

The quantitative chemical compositional analyses necessary for thermobarometric calculations were performed on a Cameca SX-100 electron microprobe (EMP) analyzer at the University of Tennessee. Real-time, qualitative assessment of the phases present in each sample was done using a PGT Si (Li) detector energy-dispersive spectrometer (EDS) as well as back-scatter electron (BSE) imaging. To determine the nature of compositional zoning in garnet porphyroblasts, quantitative point transects and X-ray compositional maps using wavelength-dispersive spectrometry of Mg, Ca, Mn, and Fe of select grains were conducted at 15 kV and 30 nA with a step size of 3 µm step size and 100 ms dwell time. Point analyses of phases such as staurolite, biotite, muscovite, and chlorite were conducted at 15 kV and 20 nA with a spot size of 1 µm. Plagioclase was analyzed under the same conditions, but at 10 kV. Point analyses were conducted on these phases both near and away from garnet porphyroblasts to determine any compositional heterogeneities among the respective phases throughout the sample. Both natural and synthetic compounds were used to check standards prior to analyses.

Thermobarometric calculations were performed using the Holland and Powell (1998) software THERMOCALC v.3.33 in average *P-T* mode. Activity coefficients for each phase and their respective endmembers were calculated with the AX software. Calculations were conducted in order to obtain *P-T* estimates at peak metamorphic temperatures using the *tc-ds55.txt* dataset of Holland and Powell (1998).

In order to more fully characterize the *P-T* history of the staurolite-kyanite grade samples (LP13-14 & LP09-11), *P-T* pseudosections were calculated using the free-energy minimizations of the Perplex 6.6.8 software package from Connolly (2009; updated in 2011). Bulk compositions for each sample were calculated by combining EMP compositional analyses for each phase with point counting modal analyses across the entire thin sections to quantify the percentage of each phase present (Tables 1 & 2). EMP analyses revealed no zonation or heterogeneities across the samples, so the average composition of each phase was used to calculate each bulk composition.

Although more simplified systems are often appropriate for metapelites, the *P-T* pseudosections were calculated using the MnNCKFMASTH system so as to account for the full range of components acting within the rock mass. BSE imaging revealed the absence of magnetite in each sample, so Fe^{3+} was not measured. The Holland and Powell (1998) thermodynamic dataset (updated in 2004; *hp04ver.*dat) was employed for gridded minimizations. Calculations were undertaken with no saturated components or phases. The CORK equation of state for H_2O (Holland & Powell, 1998) was used. Solution models for complex phases such as garnet, biotite, staurolite, chlorite, muscovite, feldspar and cordierite were taken from Fuhrman and Lindsey (1988), Holland and Powell (1998), Holland et al. (1998), Powell and Holland (1999), White et

Table 1: LP13-14 modal analysis and bulk composition used for pseudosection calculation. Mol % normalized to 100. See Table 1A for mineral compositions.

Modal Analysis

Phase	***Count***	***Percent***
Plagioclase	141	13.4
Biotite	351	33.3
Chlorite	55	5.2
Garnet	5	0.5
Ilmenite	5	0.5
Kyanite	86	8.2
Muscovite	265	25.1
Quartz	88	8.3
Rutile	3	0.3
Staurolite	55	5.2
Total	*1054*	*100*

Bulk Composition

	SiO_2	TiO_2	Al_2O_3	***FeO***	***MnO***	***MgO***	***CaO***	Na_2O	K_2O	H_2O	***Total***
wt. %	47.07	1.14	28.03	7.45	0.10	5.32	0.32	1.97	4.77	2.80	*98.97*
mol %	50.45	0.91	17.67	6.66	0.09	8.55	0.37	2.04	3.26	10.00	*100.00*

Table 2: LP09-11 modal analysis and bulk composition used for pseudosection calculation. Mol % normalized to 100. See Table 1A for mineral compositions.

Modal Analysis

Phase	***Count***	***Percent***
Plagioclase	38	3.8
Biotite	328	33.1
Chlorite	52	5.2
Cordierite	7	0.7
Ilmenite	5	0.5
Kyanite	54	5.5
Muscovite	65	6.5
Quartz	309	31.2
Rutile	2	0.2
Staurolite	132	13.4
Total	*991*	*100*

Bulk Composition

	SiO_2	TiO_2	Al_2O_3	***FeO***	***MnO***	***MgO***	***CaO***	Na_2O	K_2O	H_2O	***Total***
wt. %	55.98	1.13	21.75	7.83	0.07	5.32	0.04	0.67	3.43	2.11	*98.33*
mol %	59.49	0.90	13.60	6.93	0.06	8.48	0.04	0.69	2.32	7.49	*100.00*

al. (2000), and Coggon and Holland (2002). High-resolution contouring of the changes in modal proportions of specific phases and the chemical composition of garnet throughout *P-T* space was achieved through functions implemented in the Perplex 6.6.8 software package and outlined in Caddick and Thompson (2008). These results were plotted using a simple Matlab script available for download from the Perplex website.

P-T estimates

Compositional X-ray maps of garnet from sample LP13-11 show a decrease in X_{spess} from core to rim with a thin (~10 μm) inflection along the rim (Fig. 5a), likely the result of late period of retrograde net transfer (Kohn & Spear, 2000). Quartz inclusions in the core of garnet in this sample define a linear pattern that can be interpreted as an overgrowth of an early tectonic fabric. Electron microprobe results indicate that biotite, muscovite, and plagioclase near garnet and in the matrix show little compositional variation. The near-rim composition of garnet was combined with averaged compositions of biotite near garnet and muscovite and plagioclase data from throughout the matrix to calculate peak metamorphic conditions (Table 3). These data yield an estimate of 530 ± 23°C and 7.3 ± 0.9 kbar for garnet-grade rocks (Table 4).

Garnet from sample LP13-15 exhibits a slight decrease in X_{spess} from core to rim with a ~20 μm resorption rim (Fig 5b) that records retrograde net transfer (Kohn & Spear, 2000). Linear quartz and plagioclase inclusions in garnet from this sample can be interpreted as an overgrowth of an early tectonic fabric. Biotite near garnet and muscovite and plagioclase located throughout the matrix exhibit little compositional variation, so electron microprobe analyses from these phases were averaged for thermobarometric calculations. The near-rim composition of garnet was combined with these average compositions (Table 3) to calculate peak metamorphic conditions. These data yield an estimate of 527 ± 22°C and 7.5 ± 0.9 kbar (Table 4).

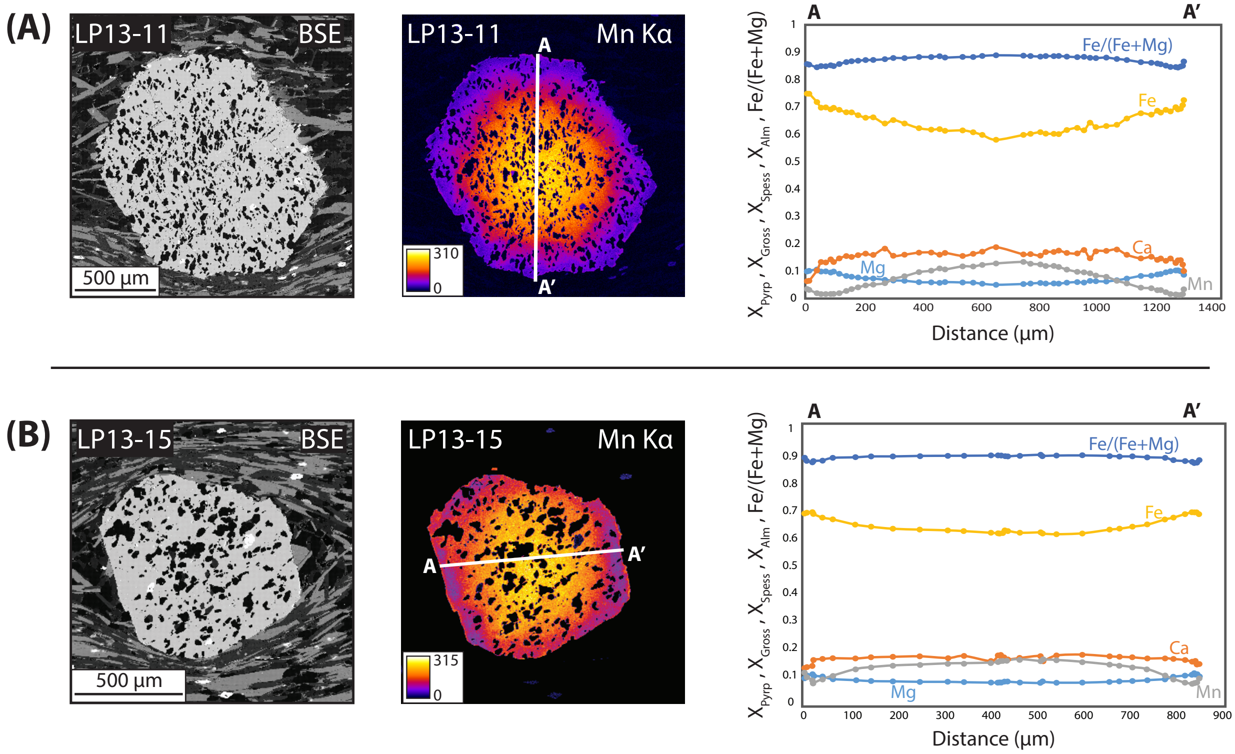

Figure 5: Garnet composition plots. Back-scatter electron (BSE) images, Mn Kα compositional maps, and point transect profiles for garnet grains in samples (A) LP13-11 and (B) LP13-15.

P-T evolution

A *P-T* pseudosection was calculated for the bulk composition of sample LP13-14 to model the *P-T* path for the growth of garnet, staurolite and kyanite present in the sample (Table 2; Fig. 6). Garnet, staurolite, and kyanite are stable in the assemblage at peak metamorphic conditions of 610 ± 31°C and 7.7 ± 1.2 kbar, as defined by the white area in Figure 6. Textural evidence of garnet occluded by kyanite (Fig. 4c) supports the interpretation of garnet growth before kyanite growth. Evidence of kyanite overgrowth of a fully developed crenulation cleavage S_2 (Fig.4b) and inclusion trails in staurolite that indicate overgrowth of only a partially developed S_2 fabric (Fig. 4a) suggests staurolite growth preceded that of kyanite. The constraints on peak metamorphic conditions are corroborated by the results of modeling the modal propor-

Table 3: Compositional data used in thermobarometric calculations. Values separated into wt. % and number of cations. Numbers in parentheses indicate the number of points averaged for each phase. Values of N/A indicate composition was not measured.

	Garnet near-rim	Biotite	Plagioclase	Muscovite		Garnet near-rim	Biotite	Plagioclase	Muscovite
LP13-11		(39)	(27)	(22)	***LP13-15***		(21)	(23)	(11)
SiO_2	37.49	36.32	60.16	47.40	SiO_2	37.38	35.44	61.85	46.83
TiO_2	0.03	1.58	N/A	0.41	TiO_2	0.05	1.72	N/A	0.49
Al_2O_3	21.23	19.35	25.14	35.75	Al_2O_3	21.25	19.15	22.90	35.49
FeO	32.32	17.31	0.19	0.94	FeO	31.56	18.79	0.31	1.22
MnO	1.33	0.04	N/A	0.01	MnO	3.00	0.20	N/A	0.01
MgO	2.84	11.38	0.04	0.69	MgO	2.64	10.34	0.02	1.10
CaO	5.21	0.04	6.61	0.02	CaO	4.96	0.06	5.31	0.01
Na_2O	0	0.18	7.79	1.01	Na_2O	0.01	0.15	8.50	0.92
K_2O	N/A	8.20	0.1	8.85	K_2O	N/A	9.16	0.07	9.39
∑	*100.45*	*99.07*	*100.03*	*99.67*	∑	*100.93*	*98.99*	*98.96*	*100.04*
Cations					*Cations*				
Si	2.99	5.45	2.68	6.24	Si	2.98	5.39	2.63	6.18
Ti	0	0.18	N/A	0.04	Ti	0.01	0.20	N/A	0.05
Al	1.99	3.42	1.32	5.55	Al	1.99	3.43	1.28	5.52
Fe	2.15	2.17	0.01	0.10	Fe	2.10	2.39	0.01	0.13
Mn	0.09	0.01	N/A	0	Mn	0.20	0.03	N/A	0.00
Mg	0.34	2.55	0	0.14	Mg	0.31	2.34	0.20	0.22
Ca	0.44	0.01	0.32	0	Ca	0.42	0.01	0.27	0.00
Na	0	0.05	0.67	0.26	Na	0.00	0.04	0.63	0.24
K	N/A	1.69	0.01	1.49	K	N/A	1.78	0.06	1.58
∑	*8.01*	*19.53*	*5.00*	*17.82*	∑	*8.02*	*19.61*	*5.08*	*13.92*

Table 4: *P-T* estimates for peak Barrovian metamorphic conditions.

Sample	*T (°C)*	*P (kbar)*	*Assemblage*	*Removed*	*Cor.*	*Fit*	*No. Rxn*	*Peak Depth (km)*
LP13-11[†]	530 ± 23	7.3 ± 0.9	grt + bt + mu + ab + qtz	cel, fcel	0.81	0.62	5	27
LP13-15[†]	527 ± 22	7.5 ± 0.9	grt + bt + mu + ab + qtz	fcel	0.79	0.86	5	28
LP13-14[α]	610 ± 31	7.7 ± 1.2	st + ky + bt + mu + ab + chl + qtz	N/A	N/A	N/A	N/A	29
LP09-11[α]	630 ± 20[β]	7.8 ± 1.1[β]	st + ky + bt + mu + ab + qtz	N/A	N/A	N/A	N/A	29

[†]Calculated using THERMOCALC in average *P-T* mode.
[α]Calculated from pseudosection modeling.
[β]These conditions were followed by a drop to 578 ± 28 °C and 4.9 ± 0.7 kbar
Peak depths calculated assuming a lithostatic pressure gradient of 3.7 km $kbar^{-1}$.
THERMOCALC output legend: Cor.---correlation coefficient; No. Rxn---number of reactions used for *P-T* estimate.

Figure 6: *P-T* pseudosection calculated for sample LP13-14. The white area represents the interpreted peak assemblage in this sample. Interpreted *P-T* path denoted by black arrow. Aluminosilicate triple point in bold. (B-D) contoured abundances of garnet, biotite, and staurolite, respectively. (E) contoured garnet Fe/(Fe+Mg) composition. Subplots (B-E) were calculated in Perplex 6.6.8 and plotted in Matlab.

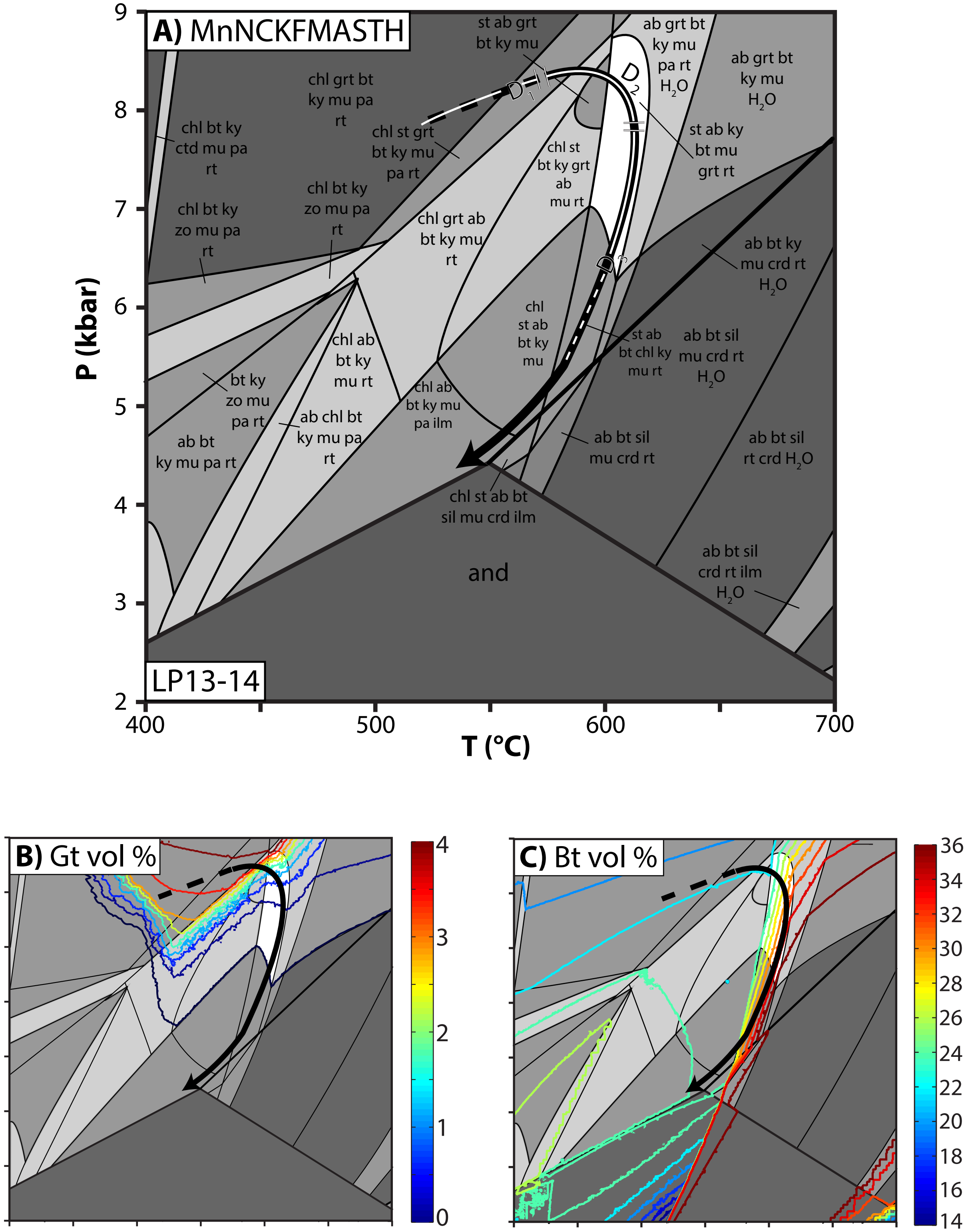
A) MnNCKFMASTH
LP13-14
P (kbar)
T (°C)
chl grt bt ky mu pa rt
chl bt ky ctd mu pa rt
chl bt ky zo mu pa rt
st ab grt bt ky mu
ab grt bt ky mu pa rt H_2O
ab grt bt ky mu H_2O
st ab ky bt mu grt rt
chl st grt bt ky mu pa rt
chl st bt ky grt ab mu rt
chl grt ab bt ky mu rt
ab bt ky mu crd rt H_2O
chl st ab bt ky mu
st ab bt chl ky mu rt
ab bt sil mu crd rt H_2O
chl ab bt ky mu rt
bt ky zo mu pa rt
ab chl bt ky mu pa rt
ab bt ky mu pa rt
chl ab bt ky mu pa ilm
ab bt sil mu crd rt
ab bt sil rt crd H_2O
chl st ab bt sil mu crd ilm
and
ab bt sil crd rt ilm H_2O
B) Gt vol %
C) Bt vol %

Figure 6.

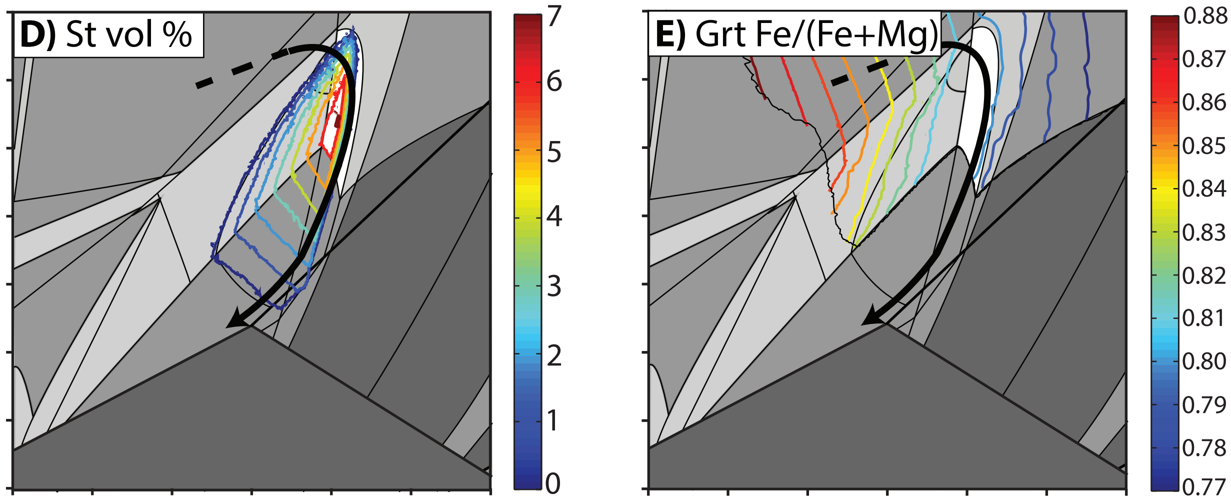

Figure 6 (*continued*).

tions of garnet, biotite, and staurolite (Figs. 6b-d), which match closely with the modal analysis across the sample. Attempts to model the latest portion of the prograde path using garnet composition proved difficult, as most of the garnet has been resorbed in this sample. Also, although the modeled Fe / (Fe+Mg) values for garnet (Fig. 6e) agree well with analyzed garnet rims in this sample, thermal modification of the garnet compositional profile cannot be ruled out. The early portion of the interpreted retrograde *P-T* path features a decrease in the modal proportion of garnet (Fig. 6b) and a transition into chlorite-bearing stability fields, consistent with textural evidence of chlorite growth at the expense of garnet. Conversely, modal abundances of biotite and staurolite are predicted to be maintained or increase immediately following peak conditions before decreasing at lower temperatures and pressures. The latter portion of the retrograde path is interpreted using two main criteria: 1) the absence of resorption textures on staurolite porphyroblasts, namely overgrowths of cordierite, a common product of staurolite breakdown at lower pressures in pelitic assemblages (e.g. Martignole & Nantel, 1982); and 2) the absence of sillimanite in the sample, which is interpreted as the rock not experiencing sillimanite growth conditions rather than kyanite metastability in the sillimanite stability field. The lack of decompression textures on Barrovian porphyroblasts as well as any unambiguous shear sense indicators in the sample suggests that this portion of the Haimanta Group was not proximal enough to the LPD during emplacement to record any modification to its burial history.

The calculated pseudosection for sample LP09-11 shows the interpreted *P-T* path for the staurolite-kyanite-grade rocks from the Haimanta Group in the NE portion of the upper Sutlej Valley (Fig. 7). Staurolite and kyanite are stable together in the assemblage at peak conditions of 630 ± 20°C and 7.8 ± 1.1 kbar, as defined by the white area in Figure 7a. The modeled pseudosection shows garnet growth along with staurolite and kyanite at peak conditions; however, since there is no garnet present in the sample or in the surrounding rocks, all garnet is assumed to have reacted out. Quartz, plagioclase, and muscovite inclusions in staurolite define a sigmoidal pattern that can be interpreted as syntectonic rotation and staurolite growth and/or an overgrowth of a crenulation. Staurolite and kyanite are overgrown by cordierite, most of which has altered to pinite (Fig. 4e), a common retrograde product of cordierite composed of muscovite and chlorite (Lal, 1969). Therefore, the early portion of the modeled retrograde *P-T* path crosses the cordierite-in reaction line and defines a path of near-isothermal decompression to 578 ± 28°C and 4.9 ± 0.7 kbar, shown in white in Fig. 7a. Both the sigmoidal inclusion trails in staurolite and the cordierite overgrowths on staurolite and kyanite indicate growth during top-down-to-the-west shearing. With decompression came an appreciable decrease in the calculated proportion of staurolite (Figs 7b & 7c), which is consistent with textural evidence of cordierite growth at the expense of staurolite. The modeled retrograde *P-T* path for this sample is markedly different from that of LP13-14, as mineral compositions and textures in sample LP09-11 indicate a distinct drop in pressure at a relatively stable temperature. The proximity of this sample to the LPD indicates that the rocks in this portion of the Haimanta Group record modification to their burial histories from dome emplacement. The aforementioned reaction textures as well as evidence for top-down-to-the-west shearing in this sample support this interpretation.

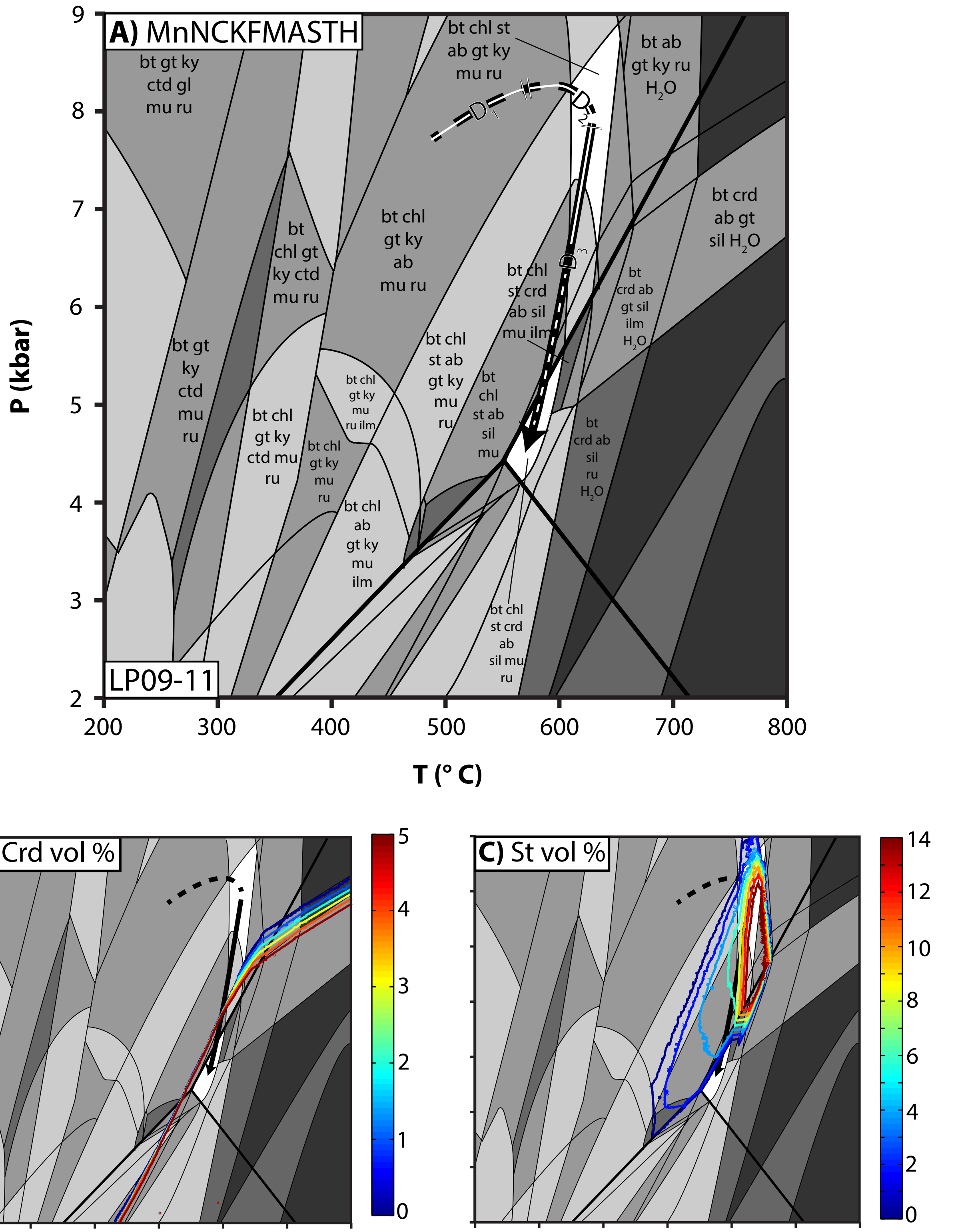

Figure 7: *P-T* pseudosection calculated for sample LP09-11. The white areas represent the interpreted assemblages from this sample. *P-T* path denoted by black arrow. Aluminosilicate triple point in bold. (B-C) contoured abundances of cordierite and staurolite, respectively. Subplots (B) and (C) were calculated in Perplex 6.6.8 and plotted in Matlab.

Chapter 3: In-situ monazite geochronology

Monazite [(LREE, Th) PO4] is a common accessory mineral in igneous and metamorphic rocks. High U and Th concentrations as well as high retentivity of radiogenic Pb in monazite (e.g. Parrish, 1990; Kohn & Malloy, 2004) make it an ideal mineral for U-Th-Pb geochronology. X-ray mapping of metamorphic monazite reveals that monazite can grow compositional domains that often reflect age domains (e.g. Zhu et al., 1997, 1999; Foster et al., 2000; Kohn et al., 2005). Advancements in geochronologic methods allow for the dating of monazite *in-situ*, which can be used to delimit periods of porphyroblast growth (e.g. Williams & Jercinovic, 2002; Chambers et al., 2009) and, where monazite is interpreted to grow along a foliation, timing of fabric development (e.g. Williams et al., 1999, 2007; Williams & Jercinovic, 2002, 2007). Zoning patterns for U, Th, and Y in monazite may form distinct domains that can be related to metamorphic reactions that occurr during monazite growth (e.g. DeWolf et al, 1993; Kohn et al., 2005; Williams et al., 2007). Y zoning in monazite has been tied to garnet and xenotime growth and breakdown; Spear and Pyle (2010) demonstrated that monazite growth is controlled by garnet in the absence of xenotime and by xenotime in the absence of garnet, and high-Y domains can develop in monazite via either garnet and/or allanite (which sequester most of the bulk Y in rocks at intermediate pressures) breakdown, dissolution of earlier monazite grains and subsequent reprecipitation along monazite rims (e.g. Seydoux-Guillaume et al., 2002), or a combination of the two.

This study uses split-stream laser ablation inductively coupled plasma mass spectrometry (LA-ICPMS). U-Th-Pb monazite geochronology is combined with REE geochemistry to delimit Barrovian porphyroblast growth and tectonic fabric development in the Haimanta Group. As monazite also sequesters LREE, trace element abundances can be used to infer the chemical conditions during monazite crystallization (e.g. Corrie & Kohn, 2008; Kohn et al., 2005; Williams et al., 1999, 2007; Stepanov et al., 2012). Previous geochronologic studies of this portion of the Haimanta Group (e.g. Chambers et al., 2009; Langille et al., 2012) did not report REE abundances for monazite, although a detailed analysis of monazite growth in the leucogranites of the LPD can be seen in Lederer et al. (2013).

Methodology

Two pelitic schist samples that were chosen for *P-T* pseudosection calculation, LP13-14 and LP09-11, were selected for geochronologic analysis. These samples are representative of the staurolite-kyanite-grade rocks of the Haimanta Group in the NE portion of Sutlej Valley that record Oligocene Barrovian metamorphism. LP09-11 also exhibits the low-pressure metamorphic overprint on Barrovian porphyroblasts that affected rocks of the Haimanta Group that are proximal to the LPD. Metamorphic monazite grains were located using the methodology outlined in Williams and Jercinovic (2002). X-ray compositional maps for Ce (Lα) of the entire thin section were collected using stage scan mapping conducted at 20 keV and 100 nA with a 33 μm step size and 30 ms dwell time on a Cameca SX-100 EMP analyzer at the University of Tennessee. For spatial reference, the Ce maps were overlain on Al (Kα) X-ray maps of the entire thin section. This method allows all monazite grains of at least ~10 μm diameter to be located and placed in a textural context. ~15 monazite grains from each sample were selected for analysis. X-ray compositional maps of Y (Lα), U (Mα), Th (Lα), and Ce (Lα), conducted at 25 kV and 40 nA with a 0.3 μm step size and 100 ms dwell time, were obtained for selected monazite grains. As compositional zoning often reflects age domains (e.g. Foster et al., 2000, 2002; Zhu et al., 1997; Schmitz & Bowring, 2000), compositional X-ray maps of individual grains allow the opportunity to assess which zone(s) to analyze as well as interpret metamorphic reactions that occurred during metamorphism (e.g. Foster et al., 2002; Cottle et al., 2009a; Spear & Pyle, 2010). Analysis spots for LA-ICPMS were chosen from the X-ray compositional maps, with preference given to discrete compositional domains, especially with respect to U and Y.

Results

Concordia diagrams plotted using Isoplot v2.4 (Ludwig, 2000) and normalized REE distributions for monazite in samples LP13-14 and LP09-11 (Fig. 8). REE abundances for monazite are normalized to McDonough and Sun (1995) chondrite composition.

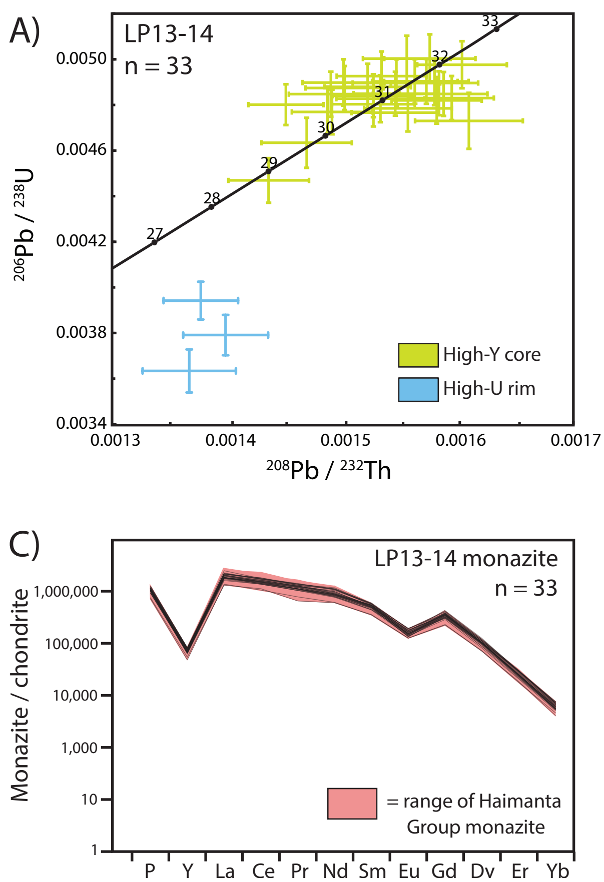

Figure 8: ^{208}Pb/^{232}Th concordia and REE distribution plots for Haimanta Group monazite. (A) & (B): Concordia diagrams for U-Th-Pb analyses of LP13-14 and LP09-11 monazite, respectively; (C) & (D): normalized REE abundances for LP13-14 and LP09-11 monazite, respectively. REE values normalized to McDonough and Sun (1995). All data obtained from LA-ICPMS analyses. See Table 3A for a summary of monazite isoptopic data.

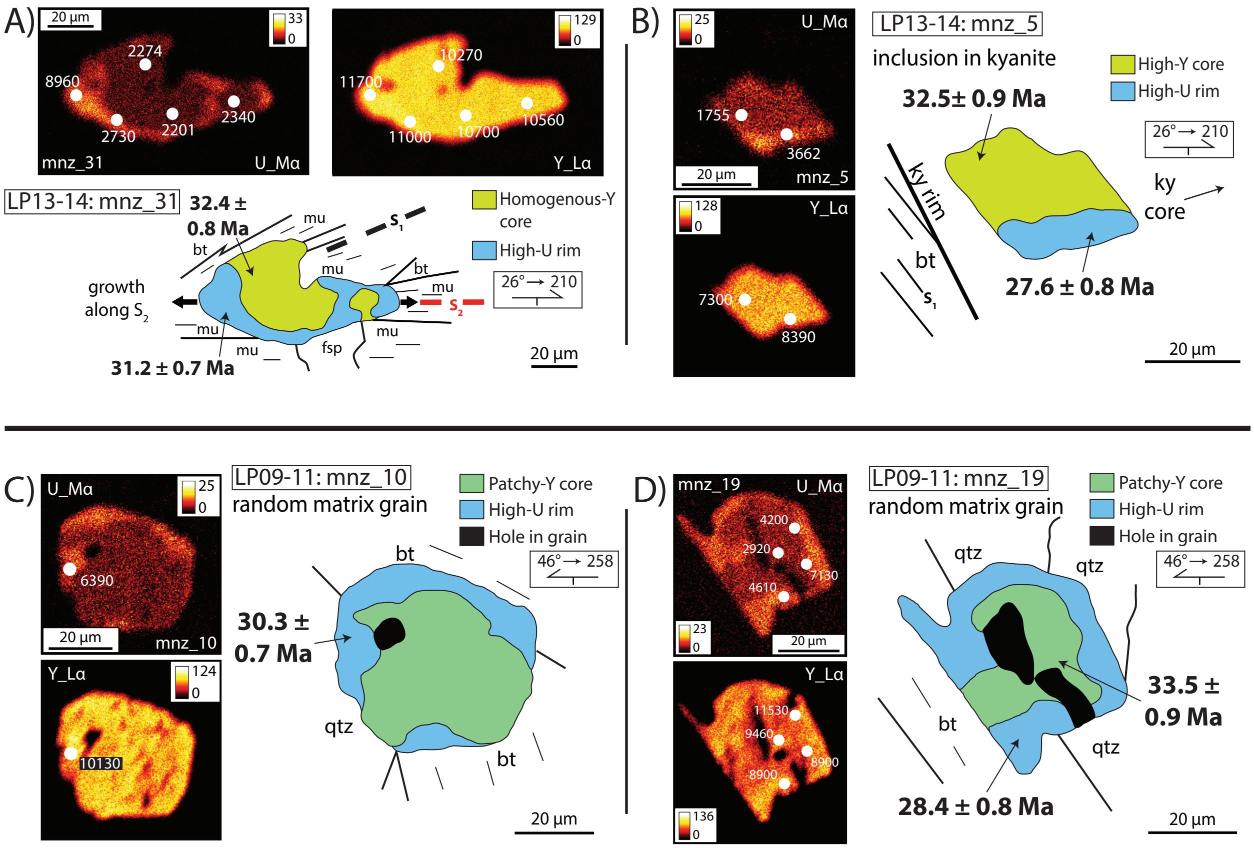

Figure 9: Representative zoning patterns for LP13-14 and LP09-11 monazite. Compositional X-ray maps for each grain are U Mα and Y Lα. Values for white dots on compositional X-ray maps show absolute abundances (in ppm) for respective elements. Colors correspond to those in Figure 8.

LP13-14

Compositional X-ray maps for monazite grains from sample LP13-14 (Figs. 9a & 9b) generally exhibit patchy Th zonation, though several matrix grains (e.g. mnz_31 and mnz_34) exhibit low-Th cores with Th concentrations that increase radially towards the rim (Fig. 2A). Y zoning across nearly all of the grains consists of homogeneous high-Y cores. High-Y domains along monazite rims occur in several grains and coincide with a relative increase in U content. Monazite grains in this sample contain low-U cores (~2000 ppm U; Th/U ratios ranging from 9–14) with several grains exhibiting wide (10–20 µm) high-U domains (> 3000 ppm U; Th/U

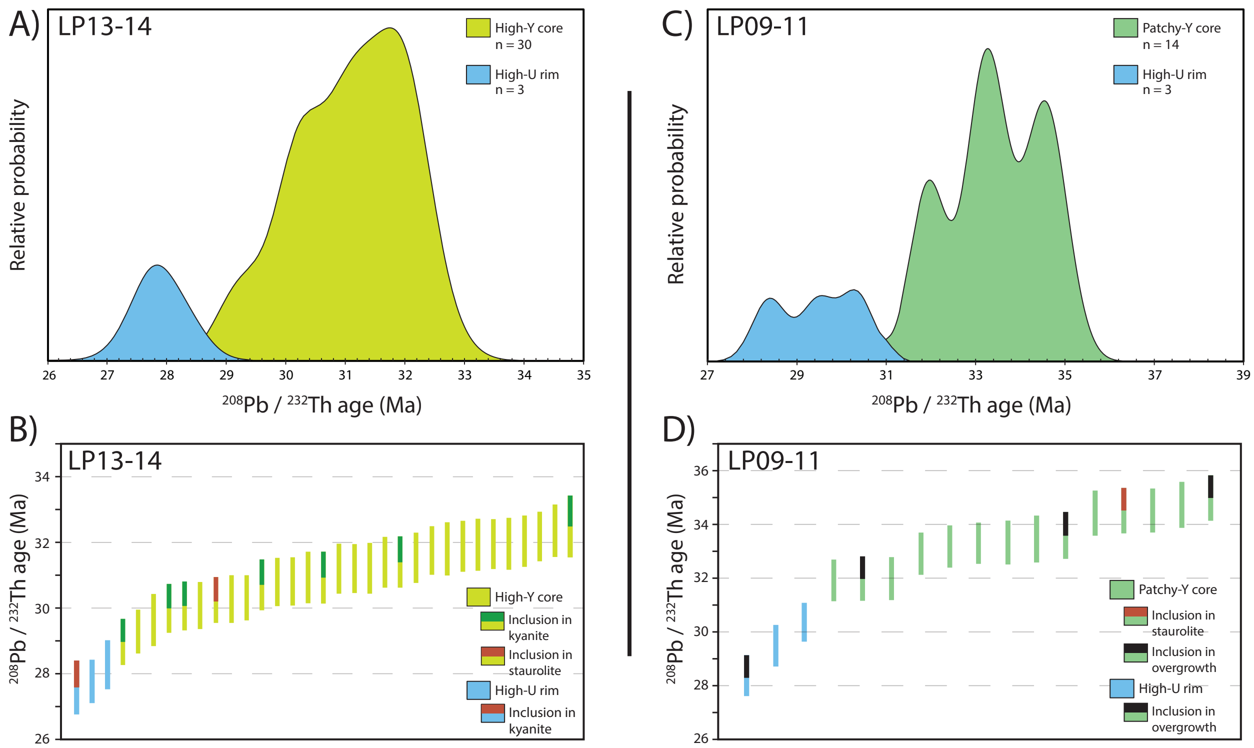

Figure 10: Probability density and weighted average age plots for LP13-14 and LP09-11 monazite. All plots report $^{208}Pb/^{232}Th$ ages. Colors correspond to those in Figures 8 and 9.

ratios of 6–7) that are localized along some portions of the grains (Figs. 9a & 9b). In general, LP13-14 monazite grains contain low abundances of light REE (La, Ce, Pr, Nd, Sm) and high abundances of heavy REE (Gd, Dy) relative to sample LP09-11 (Fig. 8c).

Analysis of the LP13-14 monazite grains with homogeneous high-Y cores yields ages that represent semi-continuous growth from 33 to 29 Ma (MSWD 5.3) (Figs. 10a & 10b). Several grains (e.g. mnz_5, mnz_32, mnz_34) feature high-U rims that are interpreted to represent a later generation of monazite and yield ages between 29 and 27 Ma (MSWD 0.86) (Figs. 9b & 10a). The high-U rim domains in mnz_31 and mnz_32 also coincide with an increase in Y content and are interpreted to have grown along the penetrative crenulation cleavage (S_2) in the sample. Analyses of these domains yield ages of 31.2 ± 0.9 Ma (mnz_31) and 27.8 ± 0.8 Ma (mnz_32), which suggests that the crenulation cleavage developed prior to ~31 Ma. The excess

Y (+ U) along monazite rims that began growing ~31 Ma may signal the onset of garnet and/or allanite breakdown in this sample (e.g. Kohn et al., 2005), dissolution of earlier monazite and subsequent reprecipitation along high-Y domains (e.g. Seydoux-Guillaume et al., 2002), or a combination of the two. The high-U rim analyses consistently plot below the concordia (Fig. 8a), suggesting ^{206}Pb loss. $^{208}Pb/^{232}Th$ ages do not consider ^{206}Pb, however, so these ages are not affected (e.g. Langille et al, 2012). Only one monazite inclusion in staurolite (mnz_1) was large enough to analyze; the grain exhibits a homogeneous high-Y core with no other discrete compositional domains and yielded an age of 30.3 ± 0.8 Ma. Several monazite inclusions in kyanite were analyzed. Ages from these grains spans the entire spectrum of ages from this sample (Fig. 10b), with the youngest age (27.6 ± 0.8 Ma) belonging to a high-U and -Y rim domain and the oldest age (32.5 ± 0.9 Ma) belonging to a homogeneous-Y core (Fig. 2A).

LP09-11

Compositional X-ray maps for monazite grains in sample LP09-11 exhibit slightly different zoning patterns than monazite grains from LP13-14. Th zoning, although patchy in some grains, occurs as high Th cores and relatively low Th mantles and rims (e.g. mnz_1, mnz_8, mnz_15) (Fig. 2A). Y generally exhibits patchy zonation, although several grains (e.g. mnz_15, mnz_18) feature low-Y cores and high-Y rims. U zoning in LP09-11 monazite grains mimics that of sample LP13-14, with low-U cores and mantles with some grains exhibiting high-U rims that coincide with high-Y domains. Monazite grains in this sample are generally enriched in light REE (La, Ce, Pr, Nd, Sm) and depleted in heavy REE (Gd, Dy) relative to sample LP13-14 (Fig.8d). Th/U ratios range from 10 (in high-Th cores) to 3 (along high-U rims).

Analyses of LP09-11 monazite grains with patchy Y cores indicate semi-continuous monazite growth from 35 to 31 Ma (seen in the stair-stepping weighted averages of Fig. 10d). Similar to LP13-14 monazite, high-U rim domains (that correspond to both Y-enriched and

Y-depleted domains) yield consistently younger ages (28 to 30 Ma) than low-U, patchy Y cores and mantles (Figs. 2c & 2d). In addition, Th zoning patterns in LP09-11 monazite grains reflect monazite formation from a single metamorphic reaction during prograde metamorphism (e.g. Kohn & Malloy, 2004). Therefore, the calculated ages from patchy Y cores are interpreted to represent a single generation of monazite growth from 35 to 31 Ma in this sample, with high U rim domains on several grains representing a second generation of crystallization following the breakdown of P- and REE-bearing phases [e.g. muscovite and chlorite (Kohn & Malloy, 2004; Chambers et al., 2009)]. Similar to LP13-14 monazite analyses, the youngest ages from this sample consistently plot below the concordia (Fig. 8b), suggesting ^{206}Pb loss. As ^{208}Pb/^{208}Th ages do not consider ^{206}Pb (e.g. Langille et al., 2012), these ages are not affected. One monazite inclusion along a resorbed staurolite rim was analyzed and yielded an age of 34.5 ± 0.9 Ma. No monazite inclusions in kyanite were large enough for analysis. Several analyzed monazite grains located in or near pinite + quartz overgrowths on staurolite porphyroblasts yielded ages that span the entire range (35 to 28 Ma) for this sample (Table 3A).

Chapter 4: Discussion

Deformation and metamorphism in the Haimanta Group

Figure 11 is a simplified illustration of the sequence of deformation and metamorphism in this portion of the Haimanta Group. Relative timing relationships of porphyroblast growth, deformation events, and fabric development in this portion of the Haimanta Group are summarized in Figure 12. Where possible, in situ U-Th-Pb ages of monazite grains were also applied to delimit the timing of phase growth and fabric development. Although the deformation events described below are noted as separate events (e.g. D_1, D_2, etc.), we interpret the sequence of deformation in the Haimanta Group as one protracted period of NE-SW-directed shortening, and the transitions between deformation events may or may not coincide with changes in tectonic setting (e.g. NE-SW extension along the STDS, orogen-parallel extension along the LPSZ, etc.). Discrete deformation event notation is used simply to describe the transposition of distinct tectonic fabrics onto one another. For a comprehensive analysis of the deformation events experienced in this portion of the Haimanta Group, see Jessup et al. (*in review*).

Burial to regional metamorphic depths (D_1) followed from the north-directed collision of India with the southern margin of Asia (e.g. Searle et al., 1987; Hodges, 2000) and led to the formation of an early tectonic foliation, S_1. Mats composed of biotite and muscovite separated by quartzofeldspathic domains delineate the S_1 foliation in the biotite zone in the central portion of Sutlej Valley (Figs. 1 & 11), and these are interpreted as syn-D_1 growth of biotite and muscovite to define an axial planar surface to F_1 folds (Fig. 12). At higher temperatures, garnet growth began after development of S_1, as evidenced by linear inclusion trails in garnet porphyroblasts that are at high angles to the matrix foliation (Figs. 3 & 5) (e.g. Chambers et al., 2009; Langille et al., 2012; Jessup et al., *in review*).

Development of the crenulation cleavage (S_2)—the pervasive fabric in the Haimanta

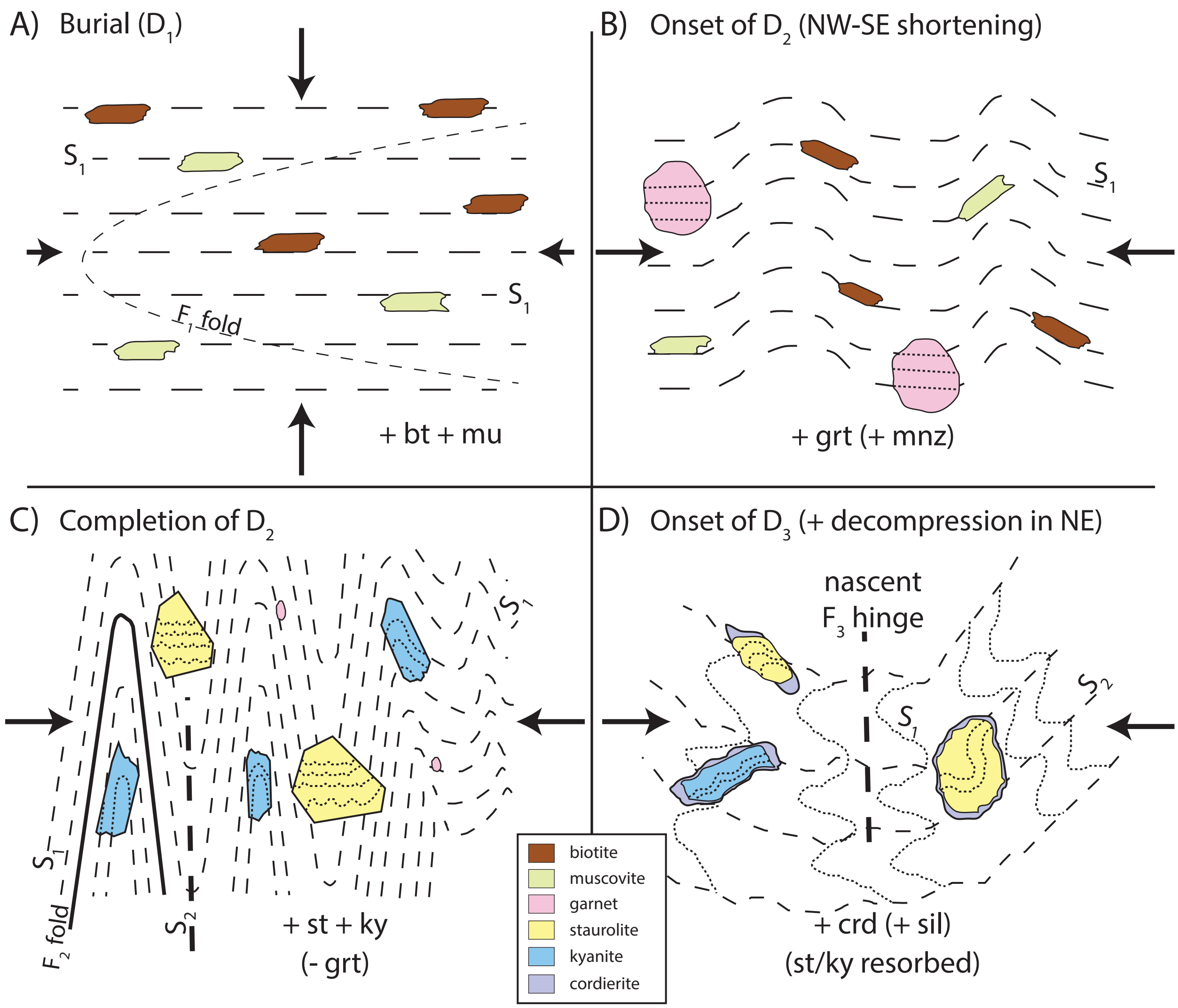

Figure 11: Schematic illustration of deformation and metamorphism in the Haimanta Group. For simplicity, viewing direction is to the NW. D_1 burial metamorphism and muscovite and biotite growth followed by protracted NE-SW shortening (D_2 & D_3) and staurolite and kyanite growth at higher temperatures. Thick black arrows denote generalized principal stress orientations.

Group—began during the final stages of garnet growth, which is interpreted by linear S_1 inclusion trails in garnet cores and sigmoidal inclusion trails along garnet rims in the central portion of the transect that mimic the crenulated S_1 foliation in the matrix (Chambers et al., 2009; Jessup et al., *in review*). These observations support the interpretation of garnet growth beginning after cessation of D_1 and continuing through the early stages of crenulation cleavage development, D_2

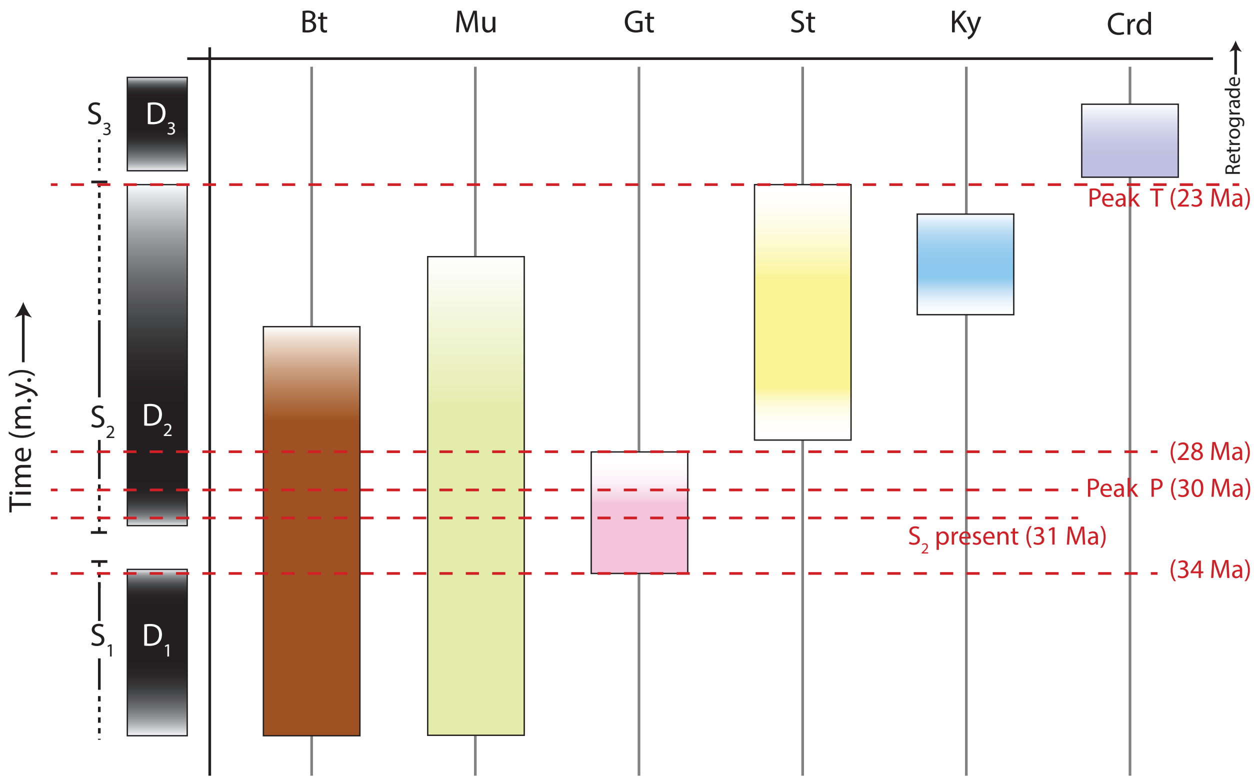

Figure 12: Relative timing of porphyroblast growth and deformation in the Haimanta Group. Red lines denote U-Th-Pb monazite age constraints from Chambers et al. (2009), Langille et al. (2012), and this study. Colors correspond to those in Figure 11.

(Figs. 11 & 12). The S_2 foliation formed as an axial planar cleavage of F_2 folds, which consistently plunge SE in this portion of the transect (Fig. 1) (Jessup et al., *in review*).

The staurolite isograd (Fig. 1b) coincides with the first appearance of kyanite. Petrographic evidence suggests that these phases grew after the onset of D_2 deformation, as poikioblastic grains of staurolite and kyanite consistently feature sigmoidal inclusion trails that mimic the pervasive F_2 crenulation cleavage, suggesting overgrowth of S_2. In sample LP13-14, inclusion trails along staurolite rims define a partially developed crenulation cleavage while inclusion trails in kyanite cores define the fully developed crenulation cleavage parallel to that of the matrix (Figs. 4a & 11), which suggests that staurolite growth preceded that of kyanite and began before the end of D_2 (Fig. 12). In sample LP13-14, kyanite occludes remnants of a resorbed garnet porphyroblast, which also suggests that kyanite was the latest phase to grow during D_2.

U-Th-Pb monazite analyses indicate that monazite growth accompanied Barrovian metamorphism. High-Y domains can grow on monazite as a result of the breakdown of garnet, which sequesters the majority of bulk Y during growth (e.g. Kohn & Malloy, 2004); however, the lack of garnet in samples LP13-14 and LP09-11 makes placing direct limits on garnet growth in this portion of the Haimanta Group difficult. $^{208}Pb/^{232}Th$ ages from high-Y rim domains on monazite—a potential product of garnet breakdown—presented in this study range from 27.6 ± 0.8 Ma to 31.2 ± 0.7 Ma, which overlap with monazite ages for Barrovian metamorphism in the Haimanta Group reported by Chambers et al. (2009) and Langille et al. (2012). The constraints on garnet growth in Figure 12 are from Chambers et al. (2009), who used Y content in monazite inclusions in garnet and in the matrix to constrain the final increments of garnet growth in the Haimanta Group in the southern portion of Sutlej Valley to ~ 28 Ma. $^{208}Pb/^{232}Th$ monazite ages indicate that high-Y cores began growing on monazite grains during prograde metamorphism—36 Ma in sample LP09-11 and 33 Ma in sample LP13-14. The breakdown of chlorite and muscovite during the garnet-in reaction likely produced the P and REE necessary to form monazite (Kohn & Malloy, 2004; Chambers et al., 2009).

In-situ monazite analysis allows for the dating of compositionally distinct domains of monazite that grew along tectonic fabrics. In sample LP13-14, analyses of high-U and -Y domains that appear to have grown parallel to mats of muscovite along the pervasive S_2 fabric yield $^{208}Pb/^{232}Th$ ages of 31.2 ± 0.9 Ma (Fig. 9) and 27.8 ± 0.8 Ma, which suggests that the S_2 fabric was present by ~ 31 Ma (Fig. 12). Chambers et al. (2009) used analyses of monazite inclusions in garnet and garnet inclusion trail geometry to conclude that peak burial and the onset of D_2 in the Haimanta Group began at ~30 Ma, about 2 Ma later than our data suggest. The youngest $^{208}Pb/^{232}Th$ ages of monazite in our samples that grew along the S_2 fabric (27–28 Ma) are used to interpret the continuation of high-U, -Y crystallization of monazite during D_2 in the Oligocene. Analyses of monazite inclusions in kyanite yield $^{208}Pb/^{232}Th$ ages that span the entire range of ages in sample LP13-14 (Fig. 10b), and the youngest age (27 Ma, from a monazite inclusion in a kyanite core) places a maximum age limit on the initiation of kyanite growth in the Haimanta Group.

The final phase of deformation, D_3, manifests as F_3 folds, which generally trend NW-SE and rotate and fold the pervasive S_2 foliation in the Haimanta Group (Jessup et al., *in review*). There is no unambiguous evidence that suggests the low-pressure overprint (cordierite + quartz + sillimanite) present along the rims of Barrovian porphyroblasts in the NE portion of Sutlej Valley (Fig. 2) coincided with D_3 deformation. Therefore, the relative timing relationship between cordierite/sillimanite growth and D_3 (Figs. 11 & 12) is ambiguous and is only meant to portray that both D_3 and cordierite (+ sillimanite) growth *postdated* Barrovian metamorphism. The youngest $^{208}Pb/^{232}Th$ ages from monazite grains located outside resorbed staurolite rims and in corditerite/pinite overgrowth zones in sample LP09-11 (~28 Ma) are interpreted as a maximum age limit for the low-pressure overprint on Barrovian metamorphism in the Haimanta Group near the LPD. The *in-situ* monazite analyses presented in this study feature a striking lack of the latest Oligocene–early Miocene (26–23 Ma) $^{208}Pb/^{232}Th$ age signature presented by Langille et al. (2012) for samples from this portion of the Haimanta Group and the LPSZ, which they used to interpret a minimum age constraint for the onset of decompression. Decompression of the NE portion of the Haimanta Group likely occurred during orogen-parallel extension and the subsequent exhumation of the LPD and may have been accompanied by rotation and folding of the S_2 foliation. Although there is no evidence in the samples presented in this study, Langille et al. (2012) documented kyanite as an inclusion in a staurolite porphyroblast with a cordierite rim in a sample collected at the confluence of the Sutlej and Spiti Rivers (LP09-162 in Fig. 1), which suggests that staurolite growth outlasted that of kyanite and continued until it was resorbed by low-pressure assemblages during decompression (Fig. 12). Evidence for the syntectonic, top-down-to-the-W rotation and growth of staurolite (Fig. 4d) and the cordierite overgrowths on staurolite porphyroblasts (Fig. 4e) in sample LP09-11 suggests that decompression may have been synchronous with D_3, but more detailed sampling and petrography are needed.

P-T-t-d evolution of the Haimanta Group

The petrographic, geochemical, and geochronologic analyses were applied to the *P-T* psuedosection modeling results for samples LP13-14 and LP09-11 (Figs. 6 & 7, respectively) in order to characterize the *P-T-t-D* paths for this portion of the Haimanta Group. The results are described below for the respective samples in order to highlight the different *P-T* histories for rocks in the central portion of the Haimanta Group (LP13-14) and those near the LPD (LP09-11).

LP13-14

Prograde metamorphism in the Haimanta Group began in the Oligocene following the crustal thickening and burial (D_1). After metamorphic biotite and muscovite growth along the S_1 fabric, initiation of the garnet-in reaction resulted in the availability of P and REE that formed monazite beginning at ~33 Ma. Petrographic evidence of garnet growth preceding that of staurolite constrains the prograde *P-T* path to pressures above 6–7 kbar, as prograde staurolite growth is predicted to precede or coincide with garnet growth around 5–6 kbar (Figs. 6b & 6d). Analyzed garnet core compositions contain Fe / (Fe+Mg) ratios around 0.82, indicating that either garnet overstepped the garnet-forming reaction by ~50°C, or garnet compositions have undergone modification (e.g. Caddick et al., 2010). Garnet rims in this sample—which are resorbed and, therefore, are interpreted not to represent the highest temperature of garnet growth preserved in this sample—feature Fe / (Fe+Mg) ratios around 0.81. Initiation of staurolite growth postdated the cessation of garnet growth (Fig. 12); therefore, the prograde *P-T* path is constrained above 8 kb along the 0.81 Fe / (Fe+Mg) contour in Figure 6d and this point represents peak burial pressure and the onset of D_2 that occurred before ~ 31 Ma. An appreciable increase in the volume percentage of biotite and staurolite (Figs. 6c & 6d) accompanied an increase in temperature after peak burial conditions, and the decrease in garnet volume percentage is consistent with the modal analysis for this sample. The assemblage of st + ab + ky + bt + mu + grt + ru was stable at peak metamorphic conditions of 610 ± 31°C and 7.7 ± 1.2 kbar as D_2 continued until the end of prograde metamorphism.

Peak conditions were followed by a moderate drop in pressure and temperature similar to those interpreted by Chambers et al. (2009) for the Haimanta Group in the southern portion of Sutlej Valley. A significant decrease in the volume percentage of staurolite following peak metamorphic conditions is predicted by the pseudosection modeling results (Fig. 6), but no resorption of staurolite is present in this sample, which suggests that initial exhumation rates were fast or that there was insufficient fluid present to drive staurolite-consuming retrograde reactions (England & Thompson, 1984; Thompson & England, 1984). Petrographic evidence of chlorite growth at the expense of biotite and garnet—as well as accessory amounts of ilmenite growth on rutile—is the only evidence of retrograde metamorphism in this sample. Therefore, the modeled retrograde path continues into chlorite- and ilmenite-bearing fields and is limited to pressures above the sillimanite and andalusite stability fields based on the lack of those phases in this sample. The interpreted *P-T* path for LP13-14 is similar to that for the Haimanta Group rocks to the south (Chambers et al., 2009), and is interpreted as the representative path followed by the Haimanta Group rocks not affected by exhumation of the LPD.

LP09-11

The modeled *P-T* evolution of the Haimanta Group rocks near the LPD differs markedly from that of the rocks to the SW. Monazite with relatively low Th cores and mantles began growing during prograde metamorphism at ~35 Ma. As there is no evidence for monazite replacement of allanite in this sample (e.g. Bollinger & Janots, 2006) and it is assumed that the breakdown of muscovite and chlorite during the garnet-in reaction produced the P and REE necessary for monazite formation (e.g. Chambers et al., 2009), this age is interpreted as a minimum age limit for the initiation of garnet growth in this sample. The lack of garnet—which is assumed to have reacted out—in this sample makes modeling the prograde *P-T* path difficult; however, we hesitantly assign peak burial conditions above ~ 8 kbar and that the staurolite-in reaction (Fig. 7c) occurred below ~ 600°C, signaling the end of garnet growth and the start of D_2. This is based on the petrographic evidence for garnet growth preceding that of staurolite in nearby outcrops (as well as throughout the staurolite-kyanite-grade rocks in the Haimanta Group). D_2 continued until the end of prograde metamorphism, which ended with the assemblage of bt + chl + st + ab + gt + ky + mu + ru stable at peak metamorphic conditions of 630 ± 20°C and 7.8 ± 1.1 kbar.

Where the interpreted *P-T* paths differ the most is during D_3 and retrograde metamorphism, which is significant in this sample. Following peak metamorphic conditions, the modal amount of staurolite decreases significantly (Fig. 7c), consistent with the petrographic evidence of staurolite resorption portrayed in Figure 4. Any remaining garnet likely reacted out to form biotite + chlorite during the early stages of D_3, and staurolite and kyanite were consumed by cordierite-forming reactions after ~28 Ma. Although the interpreted *P-T* path crosses into the sillimanite stability field, there is no sillimanite present in this sample, potentially because kyanite was essentially "buffered" by the cordierite that had formed along its rim (Xia et al., 2009). Perplex pseudosection results for LP09-11 predict the retrograde assemblage of bt + chl + st + crd + ab + sil + mu + ru (white area in Fig. 7) to be stable at conditions of 578 ± 28°C and 4.9 ± 0.7 kbar, delineating a retrograde path of near-isothermal decompression similar to that presented for rocks of the LPD by Langille et al. (2012).

Implications for exhumation of the Haimanta Group

Figure 13 provides a summary of the quantitative (thermobarometric calculation and *P-T* pseudosection modeling) and qualitative (petrographic) interpretations for the *P-T-t-D* evolution of the metapelitic rocks in the central and NE portions of the Haimanta Group. From sample LP09-11 towards the NE, a gradient in the intensity of the low-pressure overprint on Barrovian assemblages occurs that increases with proximity to the LPD. Sample LP13-14 [and the rocks in the southern portion of Sutlej Valley that Chambers et al. (2009) presented *P-T* paths for] represents the *P-T* evolution of Haimanta Group rocks not affected by the orogen-parallel exhumation of the LPD.

Cordierite is not an uncommon mineral in metapelitic rocks (e.g. Martignole & Nantel, 1982; Brown & Earl, 1983; Whittington et al., 1998; Norlander et al., 2002) and its occurrence in and around gneiss domes in the Himalaya has been well documented (e.g. Zeitler et al., 1993; Teyssier & Whitney, 2002; Whitney et al., 2004). At amphibolite-facies conditions, cordierite is only stable below 5–6 kbar (e.g. Holland & Powell, 1998; White et al., 2007), consistent with the cordierite-in reaction predicted by the pseudosection for sample LP09-11 (Fig. 7). The interpreted retrograde *P-T* path for sample LP09-11—for the segment immediately following peak conditions of 630 ± 20°C and 7.8 ± 1.1 kbar—describes a path of near-isothermal decompression across the cordierite-in reaction line to 578 ± 28°C and 4.9 ± 0.7 kbar. If a lithostatic pressure gradient of 3.7 km $kbar^{-1}$ is applied to these conditions, the rocks in this portion of Sutlej Valley describe a metamorphic field gradient of ~5°C km^{-1} during the initial stages of decompression from depths of 29–18 km. Chambers et al. (2009) estimated the initial exhumation rates for the Haimanta Group rocks to the SW at ~ 1.33 mm $year^{-1}$ from 30 to 13 Ma between peak burial depths at 30 km and 7 km (samples 8 and 14 in Figure 1b)—equivalent to a metamorphic field gradient of ~13°C km^{-1} along a retrograde *P-T* path with similar geometry to that of sample LP13-14 in Figure 6.

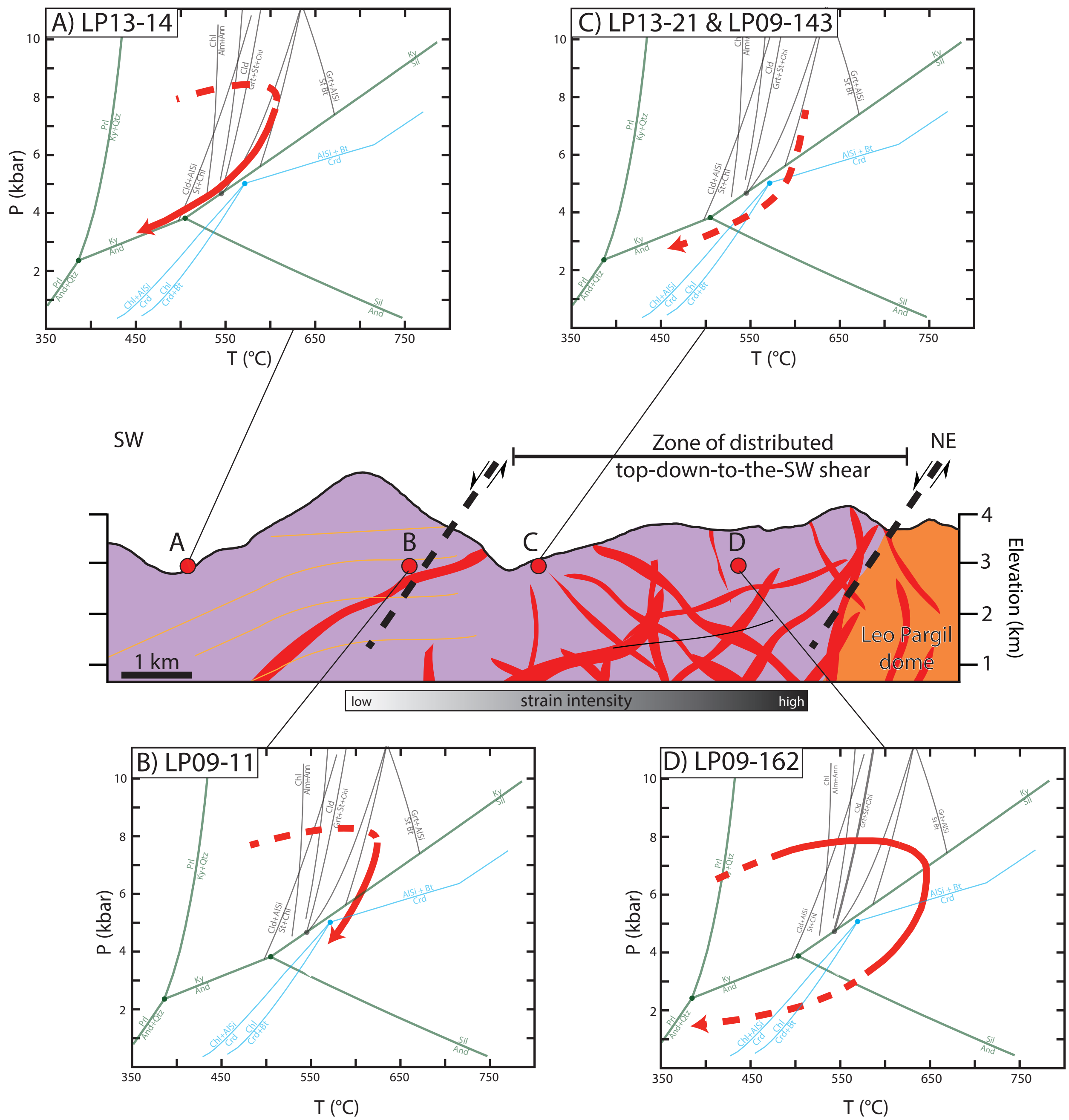

Figure 13: Synoptic diagram of *P*-*T* evolution of Haimanta Group rocks near the LPD. Colors on cross section correlate with those in Figure 1. *P*-*T* paths overlain on petrogenetic grid from Holland & Powell (1998). (A) Moderately dipping retrograde *P*-*T* path for rocks in central portion of Sutlej Valley calculated by pseudosection modeling for sample LP13-14; (B) thru (D) Haimanta Group rocks near LPD follow increasingly steep retrograde *P*-*T* paths interpreted from intensity of low-pressure overprint on staurolite and kyanite porphyroblasts and pseudosection modeling. *P*-*T* path in (D) modified from Langille et al. (2012) for sample collected near the confluence of Sutlej and Spiti Rivers near the LPD.

The transition in the Haimanta Group between the rocks in the SW and central portions of Sutlej Valley and those in the NE coincides with the occurrence of leucogranite dikes and sills associated with partial melting and emplacement of the LPD (Thiede et al., 2006; Langille et al., 2012; Lederer et al., 2013) (Fig. 1). The dikes and sills range in size from cm- to m-scale and some feature a tectonic fabric that mimics the foliation in the intruded Haimanta Group rocks, suggesting pre-, syn-, and post-kinematic emplacement (Langille et al., 2012; Lederer et al., 2013). For a detailed review of the timing of partial melting and metamorphism associated with the leucogranite dikes and sills around the LPD, see Lederer at al. (2013). The positive slope of the cordierite-in reaction line in *P-T* space (Figs. 7c & 13) implies that cordierite growth requires an increase in temperature and/or a decrease in pressure (e.g. Pereira & Bea, 1994). Cordierite + sillimanite overgrowths on Barrovian assemblages along the western flank of the LPD are attributed to heat influx from leucogranite intrusion maintaining near-isothermal conditions during the onset of exhumation before 23 Ma (Langille et al., 2012). Similarly, the leucogranite dikes and sills that intrude the NE portion of the Haimanta Group in Sutlej Valley likely enabled cordierite growth as temperatures remained above ~550°C during decompression to pressures below 5 kbar.

Another product of leucogranite intrusion in this portion of the Haimanta Group is the potential weakening of the crust due to advection of molten material and increased heat at lower pressures (e.g. Schulmann et al., 2002, 2008; Jamieson et al., 2011). Partial-melting—which can significantly reduce the effective strength of the crust (e.g. Rosenberg & Handy, 2005)—in the mid-to-lower crust between 23 and 18 Ma has been linked to strain localization along the LPSZ (e.g. Langille et al., 2012, 2014) and the subsequent decompression melting and orogen-parallel exhumation of the LPD. The LPSZ on the western flank of the LPD is comprised of staurolite-kyanite schist and a ~700-m-thick section of sheared quartzite, marble, and leucogranite that records the orogen-parallel, top-down-to-the-west exhumation of the LPD (e.g. Thiede et al., 2006; Langille et al., 2012, 2014). The high-strain LPSZ does not continue around the southern margin of the dome (Fig. 1); however, we interpret the ~5-km-thick section of the Haimanta Group intruded by leucogranite dikes in Sutlej Valley to have accommodated (a relatively minor amount of) top-down-to-the-SW shear between the Haimanta Group and the LPD [the migmatitic rocks of which Langille et al. (2012) hesitantly assigned to the GHS] during exhumation (Fig. 13). Although there is a lack of strong, unambiguous shear-sense indicators in this portion of the Haimanta Group (Fig. 2), partial melting within the LPD and heat influx from leucogranite dike intrusion likely weakened the crust sufficiently for strain localization.

This can be seen in the trajectory of retrograde *P-T* paths across this zone (Fig. 13). Sample LP13-14, from the central portion of the Haimanta Group, followed a moderately sloped *P-T* trajectory during exhumation (Fig. 13a). Beginning with sample LP09-11 and moving NE towards the LPD, samples LP13-21, LP09-143, and LP09-162 (from Langille et al., 2012) followed increasingly steep decompression *P-T* paths (Figs. 13b–d) as indicated by the intensity of the low-pressure overprint on Barrovian metamorphism and pseudosection modeling results. LP09-162 shows shear bands and strain shadows on albite that record top-down-to-the-SW shearing, likely due to proximity to the LPD. Although the differences in the retrograde *P-T* trajectories between the central and NE portion of the Haimanta Group are stark, the transition between the two zones is gradational, as there is no obvious evidence for a tectonic boundary. Similar to other localities in the Himalaya (e.g. the Gurla Mandhata core complex, the Ama Drime massif), the majority of strain and displacement was accommodated along orogen-perpendicular shear zones and faults (e.g. Murphy et al., 2002; Jessup et al., 2008; Jessup & Cottle, 2010; Cottle et al., 2009). The proximity of the LPD to the Karakoram fault system (Fig. 1) likely contributed to the tectonic setting that favored orogen-parallel extension (e.g. Thiede et al., 2006; Hintersberger et al., 2010; 2011; Langille et al., , 2014) and the differential partitioning of strain along the west- and southwest- margins of the LPD.

Summary and conclusions

Thermobarometric calculations for the Haimanta Group rocks in the hanging wall of the STDS indicate that crustal thickening following the collision of India and Asia led to Barrovian metamorphism above 600°C and 7 kbar at staurolite- and kyanite-grades. These conditions were followed by exhumation along moderately sloped *P-T* paths for rocks in the SW and central portions of Sutlej Valley. In contrast, the rocks to the NE near the LPD, experienced near-isothermal decompression during the initial stages of exhumation, as low-pressure assemblages (cordierite + sillimanite) overgrew Barrovian porphyroblasts. The gradient of the intensity of the low-pressure overprint, shear sense indicators, and the steepness of retrograde *P-T* paths for Haimanta Group rocks that increase with proximity to the LPD indicate that this zone describes a wide zone of distributed top-down-to-the-SW shear that juxtaposes the Haimanta Group against the migmatites and gneisses of the LPD, which correlate to the GHS. This study also presents new *in-situ* monazite geochronology results that place further constraints on porphyroblast growth and fabric development within the Haimanta Group.

P-T pseudosection modeling is a powerful tool for geologists and allows for the interpretation of the *P-T* evolution of rocks that are not ideal for conventional thermobarometric methods (e.g. rocks that lack garnet). This study shows that the differences in *P-T* paths followed by rocks within the same unit (the Haimanta Group) have implications for the emplacement of the LPD and the evolution of this portion of the Himalaya in general. Although this study serves to fill in gaps in the thermobarometric and geochronologic data for this region, more detailed work needs to be done. For example, in order to fully characterize the boundary between the LPD and the Haimanta Group in Sutlej Valley, detailed sampling and thermobarometry across the zone marked by leucogranite intrusion would serve to elucidate many of the questions this study presents. Also, the low-temperature (< 350°C) exhumational history of these rocks (via e.g. Ar/Ar thermochronology) would help to complete the *P-T* evolution of this portion of the Haimanta

Group.

References

Beaumont, C., Jamieson, R. A., Nguyen, M. H., and Lee, B., 2001, Himalayan tectonics explained by extrusion of a low-viscosity crustal channel coupled to focused surface denudation: Nature, v. 414, no. 6865, p. 738-742.

Bell, T. H., and Rubenach, M. J., 1983, Sequential porphyroblast growth and crenulation cleavage development during progressive deformation: Tectonophysics, v. 92, no. 1–3, p. 171-194.

Bollinger, L., and Janots, E., 2006, Evidence for Mio-Pliocene retrograde monazite in the Lesser Himalaya, far western Nepal: European Journal of Mineralogy, v. 18, no. 3, p. 289-297.

Brown, M., and Earle, M. M., 1983, Cordierite-bearing schists and gneisses from Timor, eastern Indonesia: P-T conditions of metamorphism and tectonic implications: Journal of Metamorphic Geology, v. 1, no. 2, p. 183-203.

Burg, J. P., Guiraud, M., Chen, G. M., and Li, G. C., 1984, Himalayan metamorphism and deformations in the North Himalayan Belt (southern Tibet, China): Earth and Planetary Science Letters, v. 69, no. 2, p. 391-400.

Caddick, M., and Thompson, A., 2008, Quantifying the tectono-metamorphic evolution of pelitic rocks from a wide range of tectonic settings: mineral compositions in equilibrium: Contributions to Mineralogy and Petrology, v. 156, no. 2, p. 177-195.

Caddick, M. J., Konopásek, J., and Thompson, A. B., 2010, Preservation of Garnet Growth Zoning and the Duration of Prograde Metamorphism: Journal of Petrology, v. 51, no. 11, p. 2327-2347.

Chambers, J., Caddick, M., Argles, T., Horstwood, M., Sherlock, S., Harris, N., Parrish, R., and Ahmad, T., 2009, Empirical constraints on extrusion mechanisms from the upper margin of an exhumed high-grade orogenic core, Sutlej valley, NW India: Tectonophysics, v. 477, no. 1–2, p. 77-92.

Chen, Z., Liu, Y., Hodges, K. V., Burchfiel, B. C., Royden, L. H., and Deng, C., 1990, The Kangmar Dome: A Metamorphic Core Complex in Southern Xizang (Tibet): Science, v. 250, no. 4987, p. 1552-1556.

Coggon, R., and Holland, T. J. B., 2002, Mixing properties of phengitic micas and revised garnet-phengite thermobarometers: Journal of Metamorphic Geology, v. 20, no. 7, p. 683-696.

Coleman, M. E., 1996, Orogen-parallel and orogen-perpendicular extension in the central Nepalese Himalayas: Geological Society of America Bulletin, v. 108, no. 12, p. 1594-1607.

Connolly, J. A. D., 2005, Computation of phase equilibria by linear programming: A tool for geodynamic modeling and its application to subduction zone decarbonation: Earth and Planetary Science Letters, v. 236, no. 1–2, p. 524-541.

-, 2009, The geodynamic equation of state: What and how: Geochemistry, Geophysics, Geosystems, v. 10, no. 10, p. Q10014.

Corrie, S. L., and Kohn, M. J., 2008, Trace-element distributions in silicates during prograde metamorphic reactions: implications for monazite formation: Journal of Metamorphic Geology, v. 26, no. 4, p. 451-464.

Cottle, J. M., Jessup, M. J., Newell, D. L., Horstwood, M. S. A., Noble, S. R., Parrish, R. R., Waters, D. J., and Searle, M. P., 2009, Geochronology of granulitized eclogite from the Ama Drime Massif: Implications for the tectonic evolution of the South Tibetan Himalaya: Tectonics, v. 28, no. 1, p. TC1002.

Cottle, J. M. H., M. S. A.; Parrish R. R., 2009, A new approach to single shot laser ablation analysis and its application to in-situ geochronology: Journal of Analytical Atomic Spectrometry, v. 24, p. 1355-1363.

DeWolf, C. P., Belshaw, N., and O'Nions, R. K., 1993, A metamorphic history from micron-scale 207Pb/206Pb chronometry of Archean monazite: Earth and Planetary Science Letters, v. 120, no. 3–4, p. 207-220.

Dézes, P. J., Vannay, J.-C., Steck, A., Bussy, F., and Cosca, M., 1999, Synorogenic extension: Quantitative constraints on the age and displacement of the Zanskar shear zone (northwest Himalaya): Geological Society of America Bulletin, v. 111, no. 3, p. 364-374.

Edwards, M. A., and Harrison, T. M., 1997, When did the roof collapse? Late Miocene north-south extension in the high Himalaya revealed by Th-Pb monazite dating of the Khula Kangri granite: Geology, v. 25, no. 6, p. 543-546.

England, P. C., and Thompson, A. B., 1984, Pressure—Temperature—Time Paths of Regional Metamorphism I. Heat Transfer during the Evolution of Regions of Thickened Continental Crust: Journal of Petrology, v. 25, no. 4, p. 894-928.

Foster, G., Kinny, P., Vance, D., Prince, C., and Harris, N., 2000, The significance of monazite U–Th–Pb age data in metamorphic assemblages; a combined study of monazite and garnet chronometry: Earth and Planetary Science Letters, v. 181, no. 3, p. 327-340.

Frank, W. G., B.; Guntli, P.; Miller, C., 1995, Geologic map of the Kishttwar-Chamba-Kulu region (NW Himalayas, India): Jahrbuch der Geologischen Bundesanstalt, v. 138, no. 2, p. 299-308.

Fuhrman, M. L., and Lindsley, D. H., 1988, Ternary-feldspar modeling and thermometry: American Mineralogist, v. 73, no. 3-4, p. 201-215.

Ganguly, J., Dasgupta, S., Cheng, W., and Neogi, S., 2000, Exhumation history of a section of the Sikkim Himalayas, India: records in the metamorphic mineral equilibria and compositional zoning of garnet: Earth and Planetary Science Letters, v. 183, no. 3–4, p. 471-486.

Gansser, A., 1980, The significance of the Himalayan suture zone: Tectonophysics, v. 62, no. 1–2, p. 37-52.

Gieré, R., Rumble, D., Günther, D., Connolly, J., and Caddick, M. J., 2011, Correlation of Growth and Breakdown of Major and Accessory Minerals in Metapelites from Campolungo, Central Alps: Journal of Petrology, v. 52, no. 12, p. 2293-2334.

Godin, L., Grujic, D., Law, R. D., and Searle, M. P., 2006, Channel flow, ductile extrusion and exhumation in continental collision zones: an introduction: Geological Society, London, Special Publications, v. 268, no. 1, p. 1-23.

Godin, L., Parrish, R. R., Brown, R. L., and Hodges, K. V., 2001, Crustal thickening leading to exhumation of the Himalayan Metamorphic core of central Nepal: Insight from U-Pb Geochronology and 40Ar/39Ar Thermochronology: Tectonics, v. 20, no. 5, p. 729-747.

Grujic, D., Casey, M., Davidson, C., Hollister, L. S., Kündig, R., Pavlis, T., and Schmid, S., 1996, Ductile extrusion of the Higher Himalayan Crystalline in Bhutan: evidence from quartz microfabrics: Tectonophysics, v. 260, no. 1–3, p. 21-43.

Grujic, D., Hollister, L. S., and Parrish, R. R., 2002, Himalayan metamorphic sequence as an orogenic channel: insight from Bhutan: Earth and Planetary Science Letters, v. 198, no. 1–2, p. 177-191.

Hintersberger, E., Thiede, R. C., and Strecker, M. R., 2011, The role of extension during brittle deformation within the NW Indian Himalaya: Tectonics, v. 30, no. 3, p. TC3012.

Hintersberger, E., Thiede, R. C., Strecker, M. R., and Hacker, B. R., 2010, East-west extension in the NW Indian Himalaya: Geological Society of America Bulletin, v. 122, no. 9-10, p. 1499-1515.

Hodges, K. V., 2000, Tectonics of the Himalaya and southern Tibet from two perspectives: Geological Society of America Bulletin, v. 112, no. 3, p. 324-350.

Hodges, K. V., Parrish, R. R., Housh, T. B., Lux, D. R., Burchfiel, B. C., Royden, L. H., and Chen, Z., 1992, Simultaneous Miocene Extension and Shortening in the Himalayan Orogen: Science, v. 258, no. 5087, p. 1466-1470.

Holland, T., Baker, J., and Powell, R., 1998, Mixing properties and activity-composition and relationships of chlorites in the system MgO-FeO-Al 2 O 3 -SiO 2 -H 2 O: European Journal of Mineralogy, v. 10, no. 3, p. 395-406.

Holland, T. J. B., and Powell, R., 1998, An internally consistent thermodynamic data set for phases of petrological interest: Journal of Metamorphic Geology, v. 16, no. 3, p. 309-343.

Hu, X., Sinclair, H. D., Wang, J., Jiang, H., and Wu, F., 2012, Late Cretaceous-Palaeogene stratigraphic and basin evolution in the Zhepure Mountain of southern Tibet: implications for the timing of India-Asia initial collision: Basin Research, v. 24, no. 5, p. 520-543.

Jamieson, R. A., Unsworth, M. J., Harris, N. B. W., Rosenberg, C. L., and Schulmann, K., 2011, Crustal Melting and the Flow of Mountains: Elements, v. 7, no. 4, p. 253-260.

Jessup, M. J., and Cottle, J. M., 2010, Progression from South-Directed Extrusion to Orogen-Parallel Extension in the Southern Margin of the Tibetan Plateau, Mount Everest Region, Tibet: The Journal of Geology, v. 118, no. 5, p. 467-486.

Jessup, M. J., Langille, J. M., Ahmad, T., *in review*, Structural analysis of the Haimanta Group in the upper Sutlej Valley, NW India, Tectonics.

Jessup, M. J., Newell, D. L., Cottle, J. M., Berger, A. L., and Spotila, J. A., 2008, Orogen-parallel extension and exhumation enhanced by denudation in the trans-Himalayan Arun River gorge, Ama Drime Massif, Tibet-Nepal: Geology, v. 36, no. 7, p. 587-590.

Kohn, M. J., and Malloy, M. A., 2004, Formation of monazite via prograde metamorphic reactions among common silicates: implications for age determinations: Geochimica et Cosmochimica Acta, v. 68, no. 1, p. 101-113.

Kohn, M. J., and Spear, F., 2000, Retrograde net transfer reaction insurance for pressure-temperature estimates: Geology, v. 28, no. 12, p. 1127-1130.

Kohn, M. J., Wieland, M. S., Parkinson, C. D., and Upreti, B. N., 2005, Five generations of monazite in Langtang gneisses: implications for chronology of the Himalayan metamorphic core: Journal of Metamorphic Geology, v. 23, no. 5, p. 399-406.

Lal, R. K., 1969, Retrogression of cordierite to kyanite and andalusite at Fishtail Lake, Ontario, Canada: Mineralogical Magazine, v. 37, no. 288, p. 466-471.

Langille, J. M., Jessup, M. J., Cottle, J., and Ahmad, T., 2014, Kinematic and thermal studies of the Leo Pargil Dome: Implications for synconvergent extension in the NW Indian Himalaya: Tectonics, v. 33, no. 9, p. 2014TC003593.

Langille, J. M., Jessup, M. J., Cottle, J. M., Lederer, G., and Ahmad, T., 2012, Timing of metamorphism, melting and exhumation of the Leo Pargil dome, northwest India: Journal of Metamorphic Geology, v. 30, no. 8, p. 769-791.

Langille, J. M., Jessup, M. J., Cottle, J. M., Newell, D., and Seward, G., 2010, Kinematic evolution of the Ama Drime detachment: Insights into orogen-parallel extension and exhumation of the Ama Drime Massif, Tibet–Nepal: Journal of Structural Geology, v. 32, no. 7, p. 900-919.

Larson, K. P., Godin, L., Davis, W. J., and Davis, D. W., 2010, Out-of-sequence deformation and expansion of the Himalayan orogenic wedge: insight from the Changgo culmination, south central Tibet: Tectonics, v. 29, no. 4, p. TC4013.

Le Fort, P., 1975, Himalayas: The collided range. Present knowledge of the continental arc: American Journal of Science, v. 275A, p. 1-44.

Lederer, G., Cottle, J., Jessup, M., Langille, J., and Ahmad, T., 2013, Timescales of partial melting in the Himalayan middle crust: insight from the Leo Pargil dome, northwest India: Contributions to Mineralogy and Petrology, v. 166, no. 5, p. 1415-1441.

Lee, J., Hacker, B., and Wang, Y., 2004, Evolution of North Himalayan gneiss domes: structural and metamorphic studies in Mabja Dome, southern Tibet: Journal of Structural Geology, v. 26, no. 12, p. 2297-2316.

Lee, J., Hacker, B. R., Dinklage, W. S., Wang, Y., Gans, P., Calvert, A., Wan, J., Chen, W., Blythe, A. E., and McClelland, W., 2000, Evolution of the Kangmar Dome, southern Tibet: Structural, petrologic, and thermochronologic constraints: Tectonics, v. 19, no. 5, p. 872-895.

Leech, M. L., 2008, Does the Karakoram fault interrupt mid-crustal channel flow in the western Himalaya?: Earth and Planetary Science Letters, v. 276, no. 3–4, p. 314-322.

Ludwig, K. R., 2000, Decay constant errors in U–Pb concordia-intercept ages: Chemical Geology, v. 166, no. 3–4, p. 315-318.

Martignole, J., and Nantel, S., 1982, Geothermobarometry of cordierite-bearing metapelites near the Morin anorthosite complex, Grenville Province, Quebec: The Canadian Mineralogist, v. 20, no. 3, p. 307-318.

McDonough, W. F., and Sun, S. s., 1995, The composition of the Earth: Chemical Geology, v. 120, no. 3–4, p. 223-253.

Michael P. Searle, and Laurent Godin, 2003, The South Tibetan Detachment and the Manaslu Leucogranite: A Structural Reinterpretation and Restoration of the Annapurna-Manaslu Himalaya, Nepal: The Journal of Geology, v. 111, no. 5, p. 505-523.

Murphy, M. A., Saylor, J. E., and Ding, L., 2009, Late Miocene topographic inversion in southwest Tibet based on integrated paleoelevation reconstructions and structural history: Earth and Planetary Science Letters, v. 282, no. 1–4, p. 1-9.

Murphy, M. A., Yin, A., Kapp, P., Harrison, T. M., Manning, C. E., Ryerson, F. J., Lin, D., and Jinghui, G., 2002, Structural evolution of the Gurla Mandhata detachment system, southwest Tibet: Implications for the eastward extent of the Karakoram fault system: Geological Society of America Bulletin, v. 114, no. 4, p. 428-447.

Najman, Y., Appel, E., Boudagher-Fadel, M., Bown, P., Carter, A., Garzanti, E., Godin, L., Han, J., Liebke, U., Oliver, G., Parrish, R., and Vezzoli, G., 2010, Timing of India-Asia collision: Geological, biostratigraphic, and palaeomagnetic constraints: Journal of Geophysical Research: Solid Earth, v. 115, no. B12, p. B12416.

Nelson, K. D., Zhao, W., Brown, L. D., Kuo, J., Che, J., Liu, X., Klemperer, S. L., Makovsky, Y., Meissner, R., Mechie, J., Kind, R., Wenzel, F., Ni, J., Nabelek, J., Leshou, C., Tan, H., Wei, W., Jones, A. G., Booker, J., Unsworth, M., Kidd, W. S. F., Hauck, M., Alsdorf, D., Ross, A., Cogan, M., Wu, C., Sandvol, E., and Edwards, M., 1996, Partially Molten Middle Crust Beneath Southern Tibet: Synthesis of Project INDEPTH Results: Science, v. 274, no. 5293, p. 1684-1688.

Norlander, B. H., Whitney, D. L., Teyssier, C., and Vanderhaeghe, O., 2002, Partial melting and decompression of the Thor-Odin dome, Shuswap metamorphic core complex, Canadian Cordillera: Lithos, v. 61, no. 3–4, p. 103-125.

Parrish, R. R., 1990, U–Pb dating of monazite and its application to geological problems: Canadian Journal of Earth Sciences, v. 27, no. 11, p. 1431-1450.

Pereira, M. D., and Bea, F., 1994, Cordierite-producing reactions in the Pena Negra Complex, Avila Batholith, central Spain; the key role of cordierite in low-pressure anatexis: The Canadian Mineralogist, v. 32, no. 4, p. 763-780.

Powell, R., and Holland, T., 1999, Relating formulations of the thermodynamics of mineral solid solutions; activity modeling of pyroxenes, amphiboles, and micas: American Mineralogist, v. 84, no. 1-2, p. 1-14.

Quigley, M., Liangjun, Y., Xiaohan, L., Wilson, C. J. L., Sandiford, M., and Phillips, D., 2006, 40Ar/39Ar thermochronology of the Kampa Dome, southern Tibet: Implications for tectonic evolution of the North Himalayan gneiss domes: Tectonophysics, v. 421, no. 3–4, p. 269-297.

Rosenberg, C. L., and Handy, M. R., 2005, Experimental deformation of partially melted granite revisited: implications for the continental crust: Journal of Metamorphic Geology, v. 23, no. 1, p. 19-28.

Saylor, J., DeCelles, P., Gehrels, G., Murphy, M., Zhang, R., and Kapp, P., 2010, Basin formation in the High Himalaya by arc-parallel extension and tectonic damming: Zhada basin, southwestern Tibet: Tectonics, v. 29, no. 1, p. TC1004.

Schulmann, K., Lexa, O., ŠTÍPskÁ, P., Racek, M., TajČManovÁ, L., KonopÁSek, J., Edel, J. B., Peschler, A., and Lehmann, J., 2008, Vertical extrusion and horizontal channel flow of orogenic lower crust: key exhumation mechanisms in large hot orogens?: Journal of Metamorphic Geology, v. 26, no. 2, p. 273-297.

Schulmann, K., Schaltegger, U., Jezek, J., Thompson, A. B., and Edel, J.-B., 2002, Rapid burial and exhumation during orogeny: Thickening and synconvergent exhumation of thermally weakened and thinned crust (Variscan orogen in Western Europe): American Journal of Science, v. 302, no. 10, p. 856-879.

Searle, M. P., Simpson, R. L., Law, R. D., Parrish, R. R., and Waters, D. J., 2003, The structural geometry, metamorphic and magmatic evolution of the Everest massif, High Himalaya of Nepal–South Tibet: Journal of the Geological Society, v. 160, no. 3, p. 345-366.

Searle, M. P., Windley, B. F., Coward, M. P., Cooper, D. J. W., Rex, A. J., Rex, D., Tingdong, L., Xuchang, X., Jan, M. Q., Thakur, V. C., and Kumar, S., 1987, The closing of Tethys and the tectonics of the Himalaya: Geological Society of America Bulletin, v. 98, no. 6, p. 678-701.

Seydoux-Guillaume, A.-M., Paquette, J.-L., Wiedenbeck, M., Montel, J.-M., and Heinrich, W., 2002, Experimental resetting of the U–Th–Pb systems in monazite: Chemical Geology, v. 191, no. 1–3, p. 165-181.

Simpson, C., and Schmid, S. M., 1983, An evaluation of criteria to deduce the sense of movement in sheared rocks: Geological Society of America Bulletin, v. 94, no. 11, p. 1281-1288.

Spear, F. S., and Pyle, J. M., 2010, Theoretical modeling of monazite growth in a low-Ca metapelite: Chemical Geology, v. 273, no. 1–2, p. 111-119.

Spear, F. S., Selverstone, J., Hickmott, D., Crowley, P., and Hodges, K. V., 1984, P-T paths from garnet zoning: A new technique for deciphering tectonic processes in crystalline terranes: Geology, v. 12, no. 2, p. 87-90.

Stepanov, A. S., Hermann, J., Rubatto, D., and Rapp, R. P., 2012, Experimental study of monazite/melt partitioning with implications for the REE, Th and U geochemistry of crustal rocks: Chemical Geology, v. 300–301, no. 0, p. 200-220.

Teyssier, C., and Whitney, D. L., 2002, Gneiss domes and orogeny: Geology, v. 30, no. 12, p. 1139-1142.

Thiede, R. C., Arrowsmith, J. R., Bookhagen, B., McWilliams, M., Sobel, E. R., and Strecker, M. R., 2006, Dome formation and extension in the Tethyan Himalaya, Leo Pargil, northwest India: Geological Society of America Bulletin, v. 118, no. 5-6, p. 635-650.

Thompson, A. B., and England, P. C., 1984, Pressure-Temperature-Time Paths of Regional Metamorphism II. Their Inference and Interpretation using Mineral Assemblages in Metamorphic Rocks: Journal of Petrology, v. 25, no. 4, p. 929-955.

Vannay, J.-C., and Grasemann, B., 2001, Himalayan inverted metamorphism and syn-convergence extension as a consequence of a general shear extrusion: Geological Magazine, v. 138, no. 03, p. 253-276.

Vannay, J.-C., Grasemann, B., Rahn, M., Frank, W., Carter, A., Baudraz, V., and Cosca, M., 2004, Miocene to Holocene exhumation of metamorphic crustal wedges in the NW Himalaya: Evidence for tectonic extrusion coupled to fluvial erosion: Tectonics, v. 23, no. 1, p. TC1014.

Vernon, R. H., 1978, Porphyroblast-matrix microstructural relationships in deformed metamorphic rocks: Geologische Rundschau, v. 67, no. 1, p. 288-305.

White, R. W., and Powell, R., 2011, On the interpretation of retrograde reaction textures in granulite facies rocks: Journal of Metamorphic Geology, v. 29, no. 1, p. 131-149.

White, R. W., Powell, R., Holland, T., and Worley, B., 2000, The effect of TiO2 and Fe2O3 on metapelitic assemblages at greenschist and amphibolite facies conditions: mineral equilibria calculations in the system K2O–FeO–MgO–Al2O3–SiO2–H2O–TiO2–Fe2O3: Journal of Metamorphic Geology, v. 18, no. 5, p. 497-511.

White, R. W., Powell, R., and Holland, T. J. B., 2007, Progress relating to calculation of partial melting equilibria for metapelites: Journal of Metamorphic Geology, v. 25, no. 5, p. 511-527.

Whitney, D. L., Teyssier, C., and Vanderhaeghe, O., 2004, Gneiss domes and crustal flow: Geological Society of America Special Papers, v. 380, p. 15-33.

Whittington, A., Harris, N., and Baker, J., 1998, Low-pressure crustal anatexis: the significance of spinel and cordierite from metapelitic assemblages at Nanga Parbat, northern Parkistan: Geological Society, London, Special Publications, v. 138, no. 1, p. 183-198.

Wiesmayr, G., and Grasemann, B., 2002, Eohimalayan fold and thrust belt: Implications for the geodynamic evolution of the NW-Himalaya (India): Tectonics, v. 21, no. 6, p. 1058.

Williams, M. L., 1994, Sigmoidal inclusion trails, punctuated fabric development, and interactions between metamorphism and deformation: Journal of Metamorphic Geology, v. 12, no. 1, p. 1-21.

Williams, M. L., and Jercinovic, M. J., 2002, Microprobe monazite geochronology: putting absolute time into microstructural analysis: Journal of Structural Geology, v. 24, no. 6–7, p. 1013-1028.

Williams, M. L., Jercinovic, M. J., and Hetherington, C. J., 2007, Microprobe Monazite Geochronology: Understanding Geologic Processes by Integrating Composition and Chronology: Annual Review of Earth and Planetary Sciences, v. 35, no. 1, p. 137-175.

Williams, M. L., Jercinovic, M. J., and Terry, M. P., 1999, Age mapping and dating of monazite on the electron microprobe: Deconvoluting multistage tectonic histories: Geology, v. 27, no. 11, p. 1023-1026.

Windley, B. F., 1983, Metamorphism and tectonics of the Himalaya: Journal of the Geological Society, v. 140, no. 6, p. 849-865.

Xia, F., Brugger, J., Chen, G., Ngothai, Y., O'Neill, B., Putnis, A., and Pring, A., 2009, Mechanism and kinetics of pseudomorphic mineral replacement reactions: A case study of the replacement of pentlandite by violarite: Geochimica et Cosmochimica Acta, v. 73, no. 7, p. 1945-1969.

Xu, Z., Wang, Q., Pêcher, A., Liang, F., Qi, X., Cai, Z., Li, H., Zeng, L., and Cao, H., 2013, Orogen-parallel ductile extension and extrusion of the Greater Himalaya in the late Oligocene and Miocene: Tectonics, v. 32, no. 2, p. 191-215.

Yin, A., 2006, Cenozoic tectonic evolution of the Himalayan orogen as constrained by along-strike variation of structural geometry, exhumation history, and foreland sedimentation: Earth-Science Reviews, v. 76, no. 1–2, p. 1-131.

Zeitler, P. K., Chamberlain, C. P., and Smith, H. A., 1993, Synchronous anatexis, metamorphism, and rapid denudation at Nanga Parbat (Pakistan Himalaya): Geology, v. 21, no. 4, p. 347-350.

Zhang, J., Ding, L., Zhong, D., and Zhou, Y., 2000, Orogen-parallel extension in the Himalaya: Is it the indicator of collapse or the product in process of compressive uplift?: Chinese Science Bulletin, v. 45, p. 114-120.

Zhu, X. K., and O'Nions, R. K., 1999, Zonation of monazite in metamorphic rocks and its implications for high temperature thermochronology: a case study from the Lewisian terrain: Earth and Planetary Science Letters, v. 171, no. 2, p. 209-220.

Zhu, X. K., O'Nions, R. K., Belshaw, N. S., and Gibb, A. J., 1997, Significance of in situ SIMS chronometry of zoned monazite from the Lewisian granulites, northwest Scotland: Chemical Geology, v. 135, no. 1–2, p. 35-53.

Appendix

Table 1A: Average mineral compositions.

Table 1A.

	Biotite	Plagioclase		Muscovite	Garnet	Staurolite	Chlorite	Cordierite	Ilmenite
		matrix	inclusions		near-rim				
LP13-11									
SiO_2	36.32	60.16	58.33	47.40	37.49	-	-	-	-
TiO_2	1.58	-	-	0.41	0.03	-	-	-	-
Al_2O_3	19.35	25.14	25.24	35.75	21.23	-	-	-	-
FeO	17.31	0.19	0.68	0.94	32.32	-	-	-	-
MnO	0.04	-	-	0.01	1.33	-	-	-	-
MgO	11.38	0.04	0.01	0.69	2.84	-	-	-	-
CaO	0.04	6.61	8.08	0.02	5.21	-	-	-	-
Na_2O	0.18	7.79	6.95	1.01	0	-	-	-	-
K_2O	8.20	0.1	0.05	8.85	N/A	-	-	-	-
∑	*99.07*	*100.03*	*99.35*	*99.67*	*100.45*	-	-	-	-
Cations									
Si	5.45	2.68	2.63	6.24	2.99	-	-	-	-
Ti	0.18	-	-	0.04	0	-	-	-	-
Al	3.42	1.32	1.34	5.55	1.99	-	-	-	-
Fe	2.17	0.01	0.03	0.10	2.15	-	-	-	-
Mn	0.01	-	-	0	0.09	-	-	-	-
Mg	2.55	0	0	0.14	0.34	-	-	-	-
Ca	0.01	0.32	0.39	0	0.44	-	-	-	-
Na	0.05	0.67	0.61	0.26	0	-	-	-	-
K	1.69	0.01	0	1.49	N/A	-	-	-	-
∑	*19.53*	*5.00*	*5.00*	*17.82*	*8.01*	-	-	-	-

Table 1A (*continued*).

	Biotite	Plagioclase		Muscovite	Garnet	Staurolite	Chlorite	Cordierite	Ilmenite
		matrix	inclusions		near-rim				
LP13-15									
SiO_2	35.44	61.85	59.14	46.83	37.38	-	-	-	-
TiO_2	1.72	-	-	0.49	0.05	-	-	-	-
Al_2O_3	19.15	22.90	24.45	35.49	21.25	-	-	-	-
FeO	18.79	0.31	0.49	1.22	31.56	-	-	-	-
MnO	0.2	-	-	0.01	3	-	-	-	-
MgO	10.34	0.02	0.01	1.1	2.64	-	-	-	-
CaO	0.06	5.31	7.32	0.01	4.96	-	-	-	-
Na_2O	0.15	8.5	7.38	0.92	0.01	-	-	-	-
K_2O	9.16	0.07	0.06	9.39	-	-	-	-	-
∑	*98.99*	*98.96*	*98.85*	*100.04*	*100.93*	-	-	-	-
Cations									
Si	5.39	2.63	2.68	6.18	2.98	-	-	-	-
Ti	0.20	-	-	0.05	0.01	-	-	-	-
Al	3.43	1.28	1.30	5.52	1.99	-	-	-	-
Fe	2.39	0.01	0.02	0.13	2.1	-	-	-	-
Mn	0.03	-	-	0	0.2	-	-	-	-
Mg	2.34	0.2	0	0.22	0.31	-	-	-	-
Ca	0.01	0.27	0.35	0	0.42	-	-	-	-
Na	0.04	0.63	0.65	0.24	0	-	-	-	-
K	1.78	0.06	0	1.58	-	-	-	-	-
∑	*19.61*	*5.08*	*5.00*	*17.92*	*8.02*	-	-	-	-

Table 1A (*continued*).

	Biotite	Plagioclase		Muscovite	Garnet	Staurolite	Chlorite	Cordierite	Ilmenite
		matrix	inclusions		near-rim				
LP13-14									
SiO_2	36.56	65.61	-	46.77	37.32	27.77	25.32	-	0.04
TiO_2	1.57	-	-	0.41	0	0.71	0.12	-	52.63
Al_2O_3	19.65	21.59	-	36.98	21.27	54.18	23.42	-	0.02
FeO	15.50	0.09	-	0.66	31.35	13.04	20.39	-	45.02
MnO	0.09	-	-	0	5.72	0.33	0.18	-	1.66
MgO	12.32	0.01	-	0.49	3.91	2.06	18.18	-	0.23
CaO	0.01	2.31	-	0.02	0.91	0.01	0.01	-	0.01
Na_2O	0.21	10.41	-	2.01	0.02	0.01	0.01	-	0
K_2O	8.73	0.07	-	7.33	-	0	0.02	-	-
∑	*98.71*	*100.07*	-	*99.26*	*100.58*	*100.47*	*91.39*	-	*99.64*
Cations									
Si	5.45	2.88	-	6.15	2.98	3.83	4.08	-	0
Ti	0.18	-	-	0.04	0	0.07	0.01	-	4.01
Al	3.45	1.12	-	5.72	2.01	8.81	4.45	-	0
Fe	1.94	0	-	0.07	2.09	1.51	2.75	-	3.81
Mn	0.01	-	-	0	0.39	0.04	0.03	-	0.14
Mg	2.74	0	-	0.11	0.47	0.42	4.36	-	0.03
Ca	0	0.11	-	0	0.08	0	0	-	0
Na	0.06	0.89	-	0.51	0	0	0	-	0
K	1.66	0	-	1.23	-	0	0.01	-	-
∑	*19.51*	*5.00*	-	*17.82*	*8.02*	*16.69*	*19.68*	-	*7.99*

Table 1A (*continued*).

	Biotite	Plagioclase		Muscovite	Garnet	Staurolite	Chlorite	Cordierite	Ilmenite
		matrix	inclusions		near-rim				
LP09-11									
SiO_2	36.67	67.85	-	45.78	-	28.01	25.34	48.75	0.02
TiO_2	1.71	-	-	0.46	-	0.66	0.12	-	52.56
Al_2O_3	19.94	20.29	-	36.65	-	54.68	23.46	33.89	0.02
FeO	14.67	0.04	-	0.65	-	12.48	20.16	8.44	45.49
MnO	0.06	-	-	0.01	-	0.27	0.12	0.01	1.28
MgO	12.35	0	-	0.47	-	1.91	18.18	8.59	0.09
CaO	0.03	0.66	-	0	-	0.01	0.01	0	0
Na_2O	0.34	11.26	-	1.96	-	0	0	0.04	0
K_2O	8.77	0.05	-	7.98	-	0	0.02	0	-
∑	*98.6*	*100.16*	-	*98.56*	-	*100.25*	*91.16*	*99.72*	*99.48*
Cations									
Si	5.45	2.96	-	6.09	-	3.85	4.08	4.93	0
Ti	0.19	-	-	0.05	-	0.07	0.01	-	4.01
Al	3.50	1.04	-	5.75	-	8.86	4.46	4.06	0
Fe	1.83	0	-	0.07	-	1.44	2.72	0.73	3.86
Mn	0.01	-	-	0	-	0.03	0.02	0	0.11
Mg	2.74	0	-	0.09	-	0.39	4.37	1.22	0.01
Ca	0.01	0.03	-	0	-	0	0	0	0
Na	0.10	0.95	-	0.51	-	0	0	0	0
K	1.66	0	-	1.36	-	0	0	0	-
∑	*19.49*	*4.99*	-	*17.92*	-	*16.65*	*19.67*	*10.94*	*7.99*

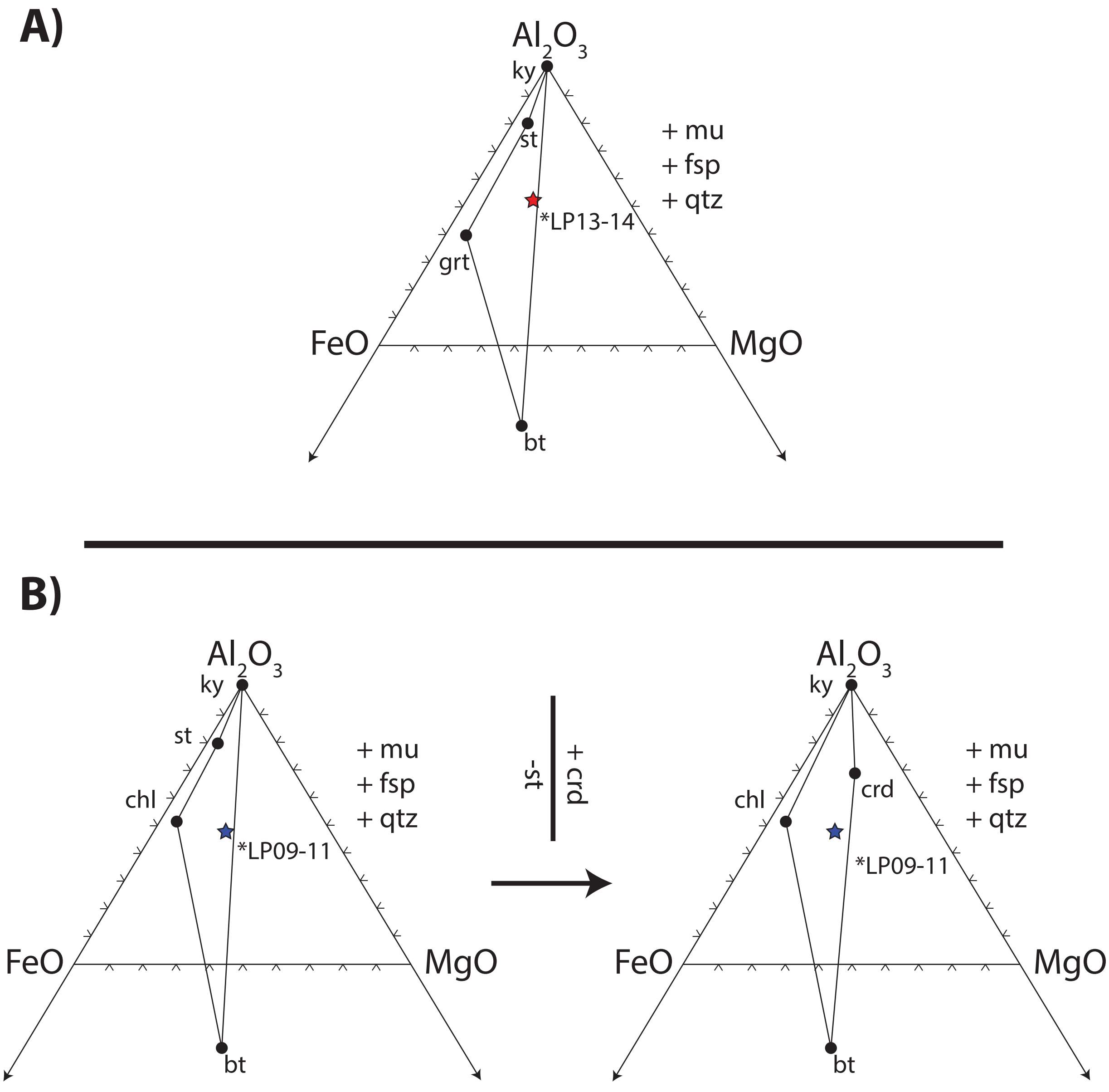

Figure 1A: LP13-14 and LP09-11 bulk chemistry and mineral composition AFM diagrams.

Table 2A: Sample locations and orientations.

Sample	Latitude	Longitude	Orientation	Surface
LP13-11	31.7464	78.5745	072/39 SE	S_1
LP13-15	31.7557	78.6006	234/14 SE	S_2
LP13-14	31.7570	78.5977	104/65 SW	S_1
LP09-11	31.7606	78.6358	168/46 SW	n/a
LP09-144	31.7586	78.6311	350/44 SW	n/a
LP13-21	31.7837	78.637	111/64 NE	S_1
LP09-143	31.7835	78.6365	n/a	n/a
LP13-23	31.7963	78.6386	015/42 NW	S_1
LP13-24	31.7965	78.6371	059/13 NW	S_1

Figure 2A: Compositional maps of metamorphic monazite.

LP13-14

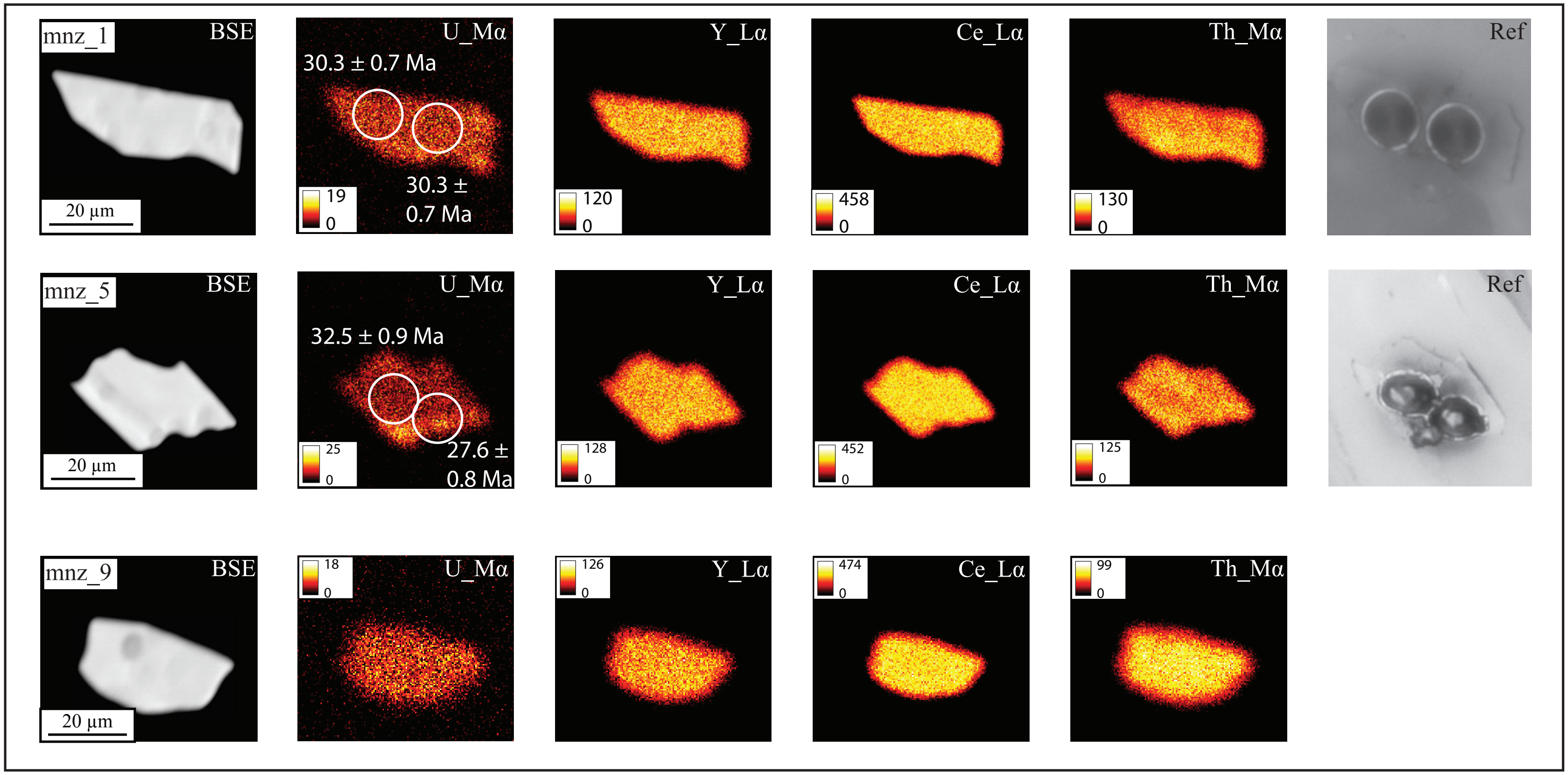

Figure 2A.

LP13-14 (*cont.*)

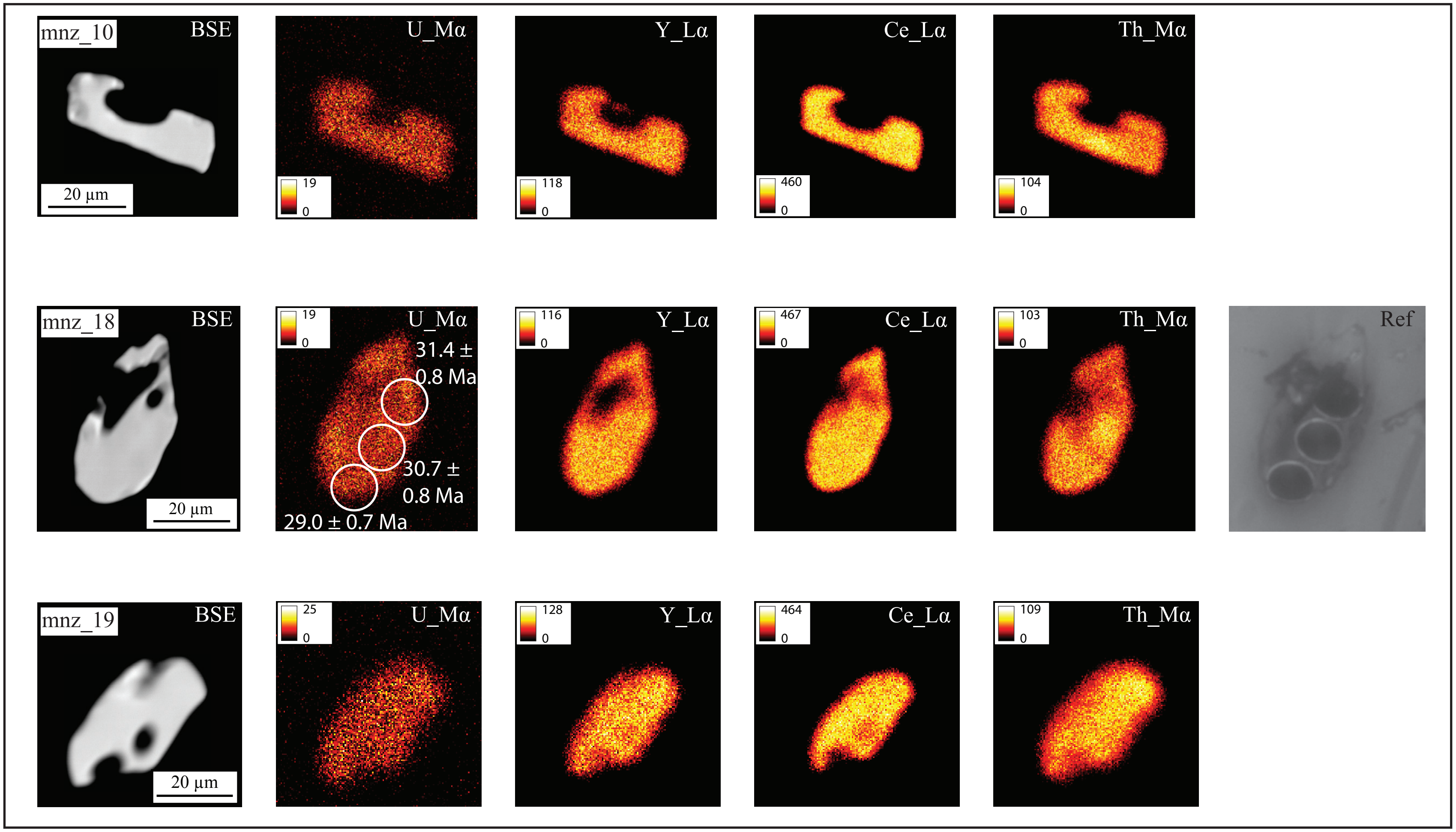

Figure 2A (*continued*).

LP13-14 (*cont.*)

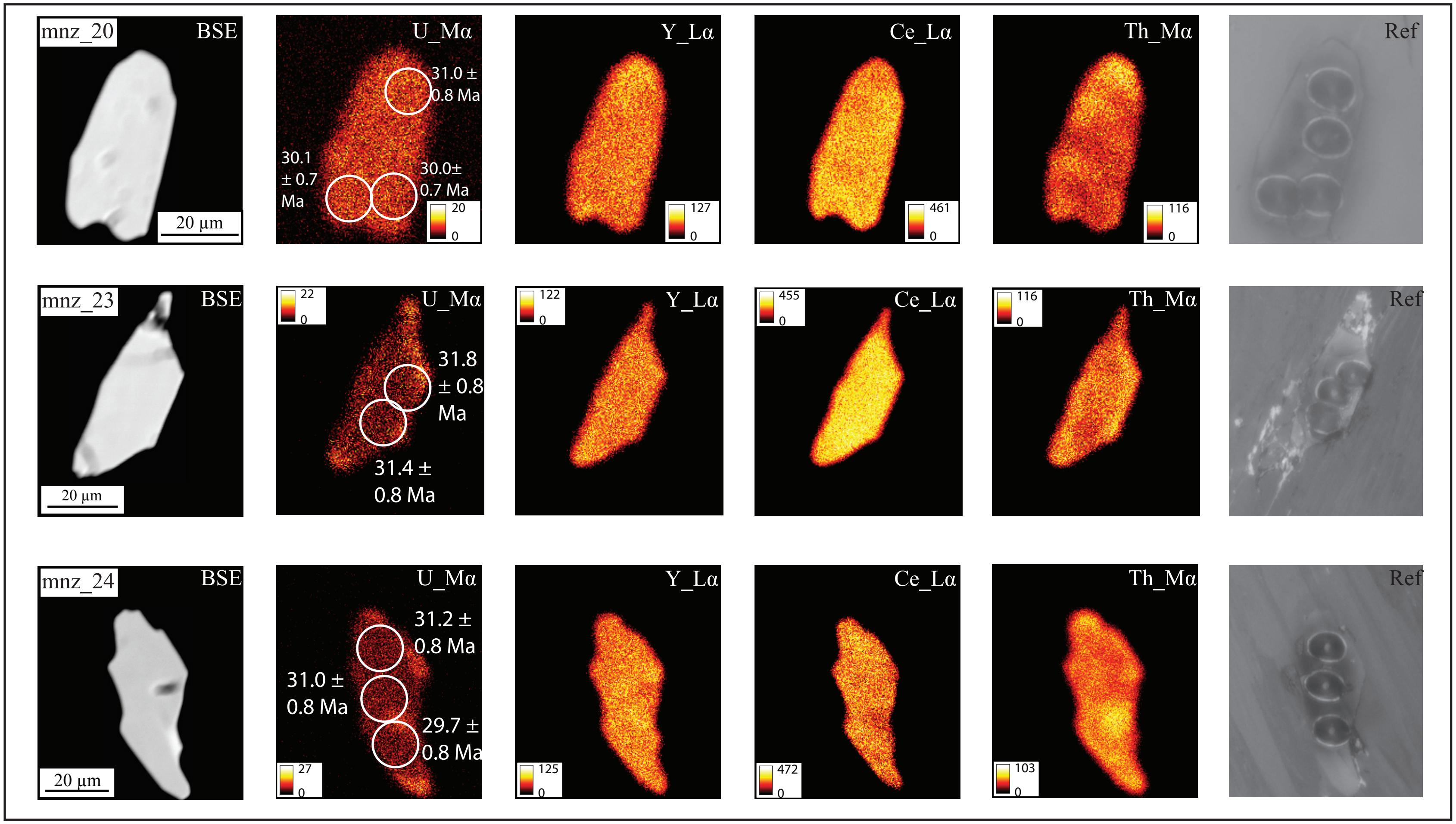

Figure 2A (*continued*).

<u>LP13-14</u> (*cont.*)

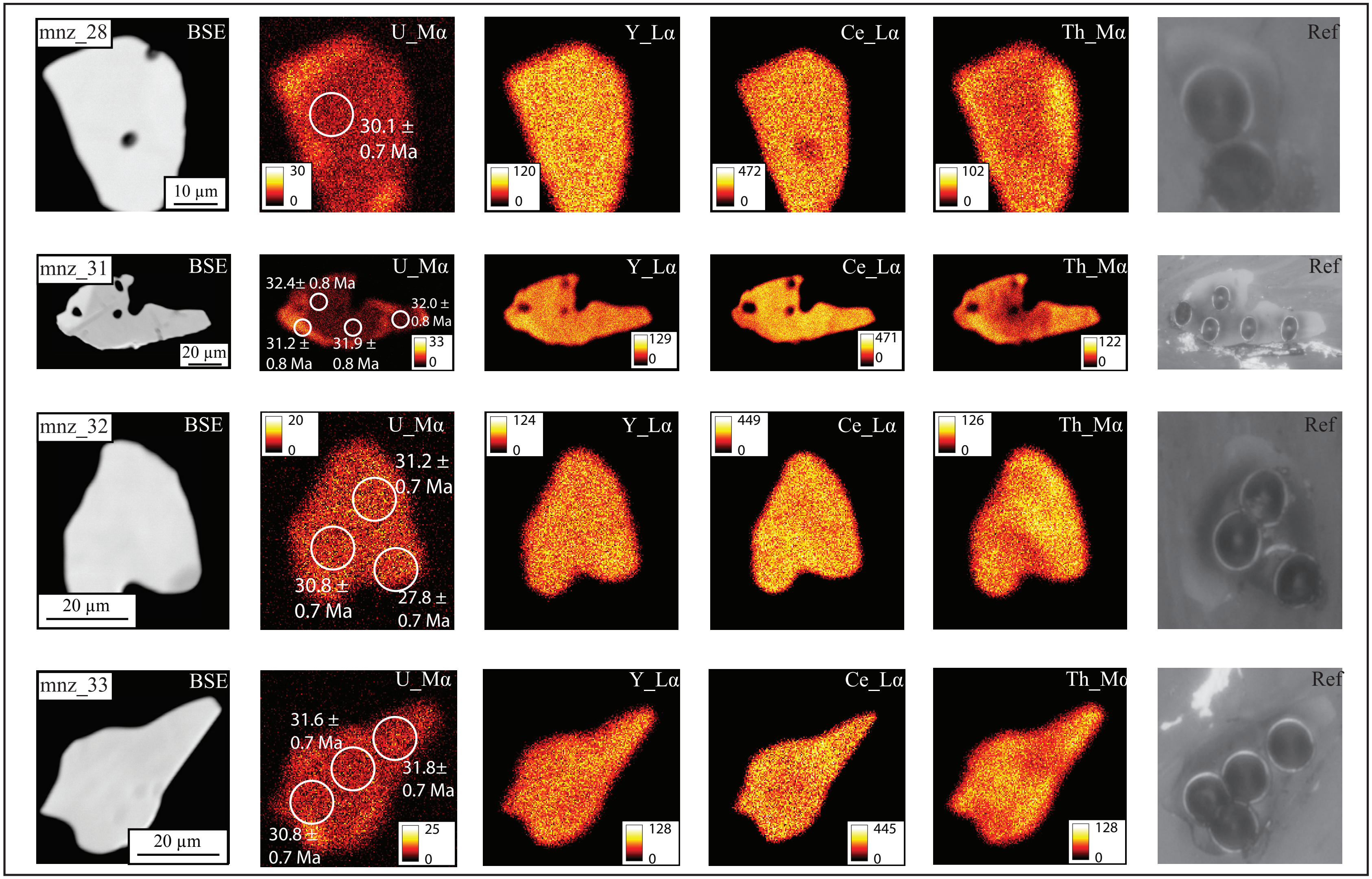

Figure 2A (*continued*).

LP13-14 (*cont.*)

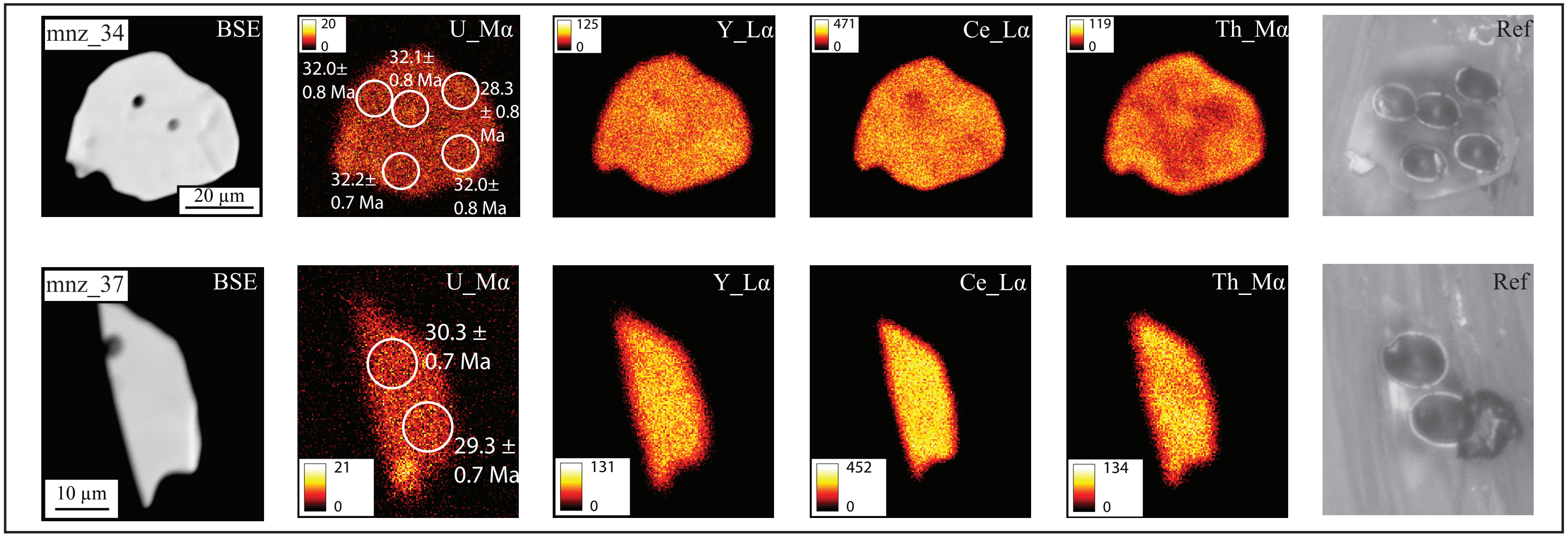

LP09-11

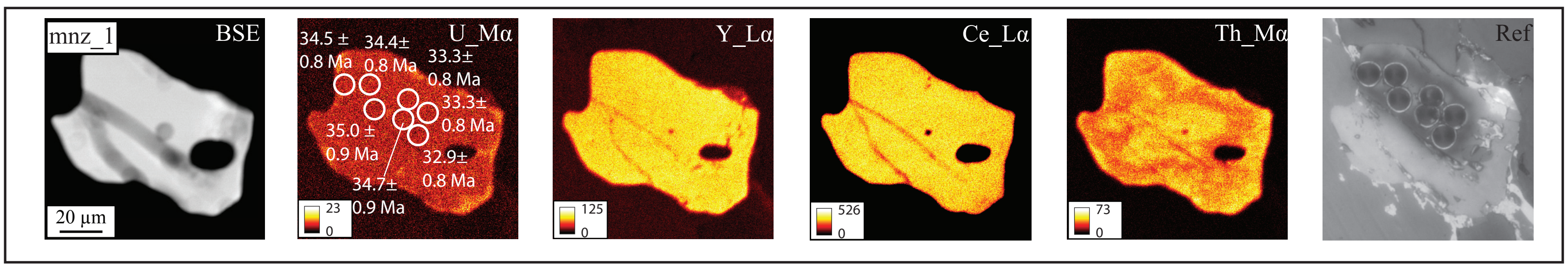

Figure 2A (*continued*).

LP09-11 (*cont.*)

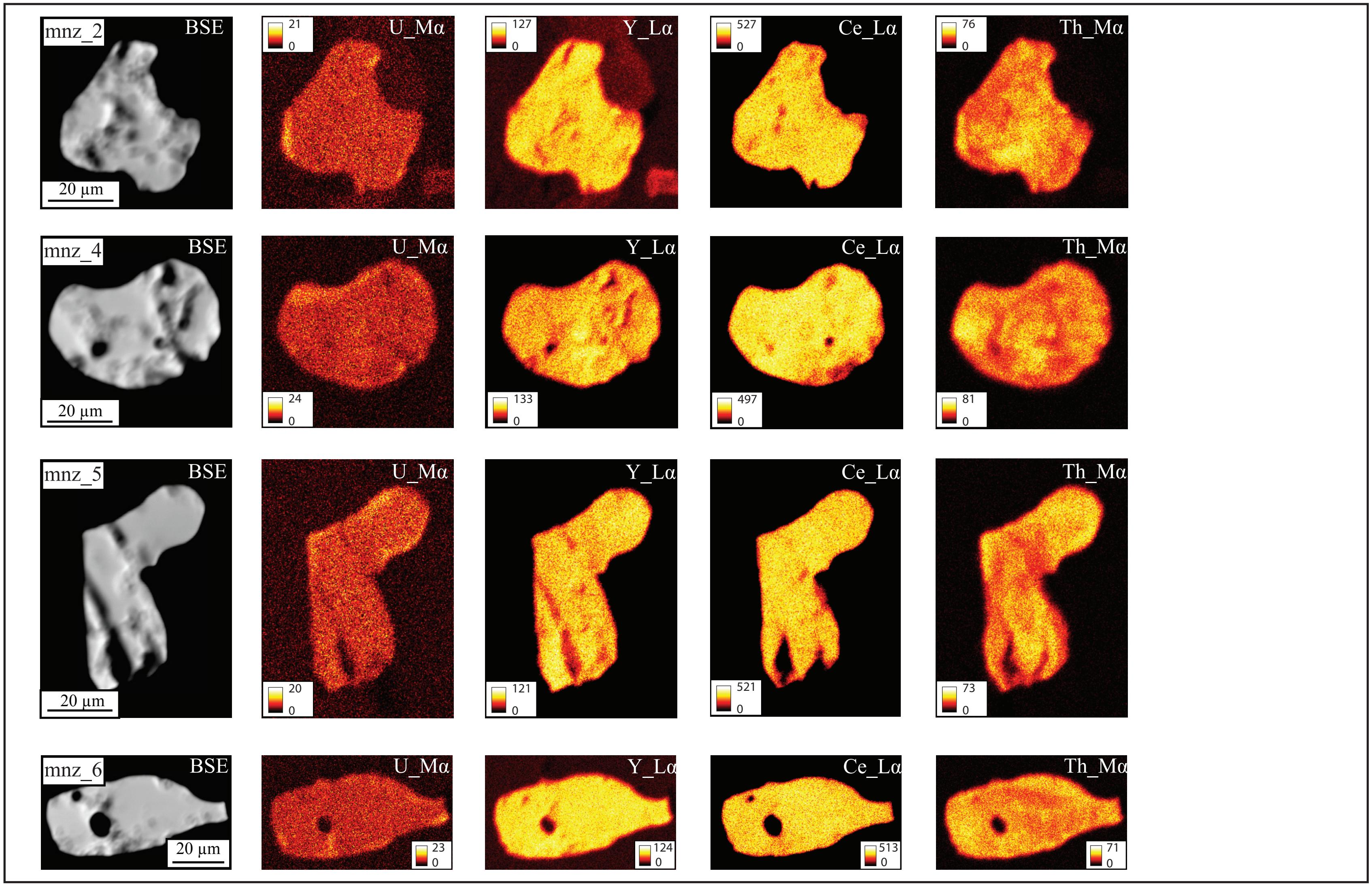

Figure 2A (*continued*).

LP09-11 (*cont.*)

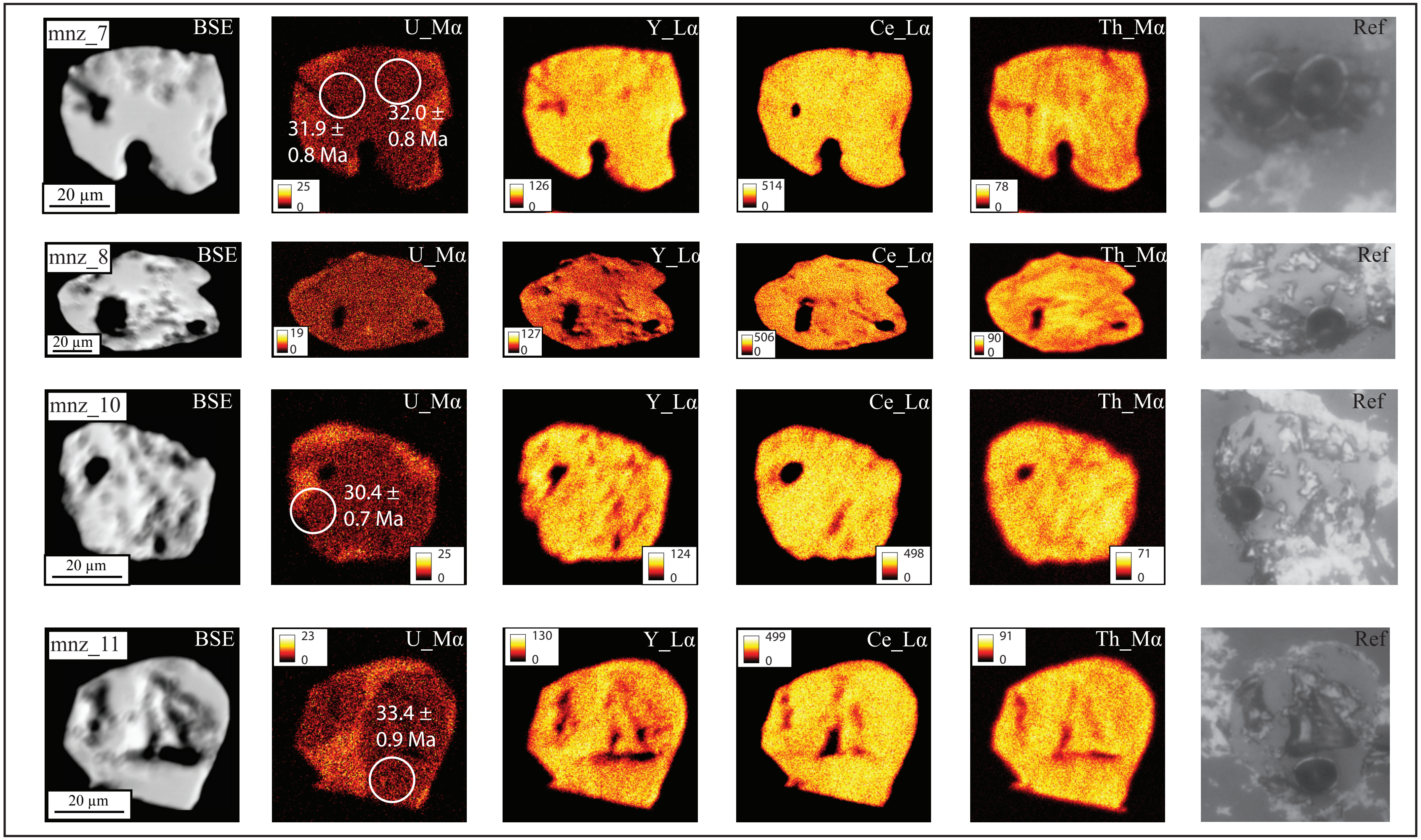

Figure 2A (*continued*).

LP09-11 (*cont.*)

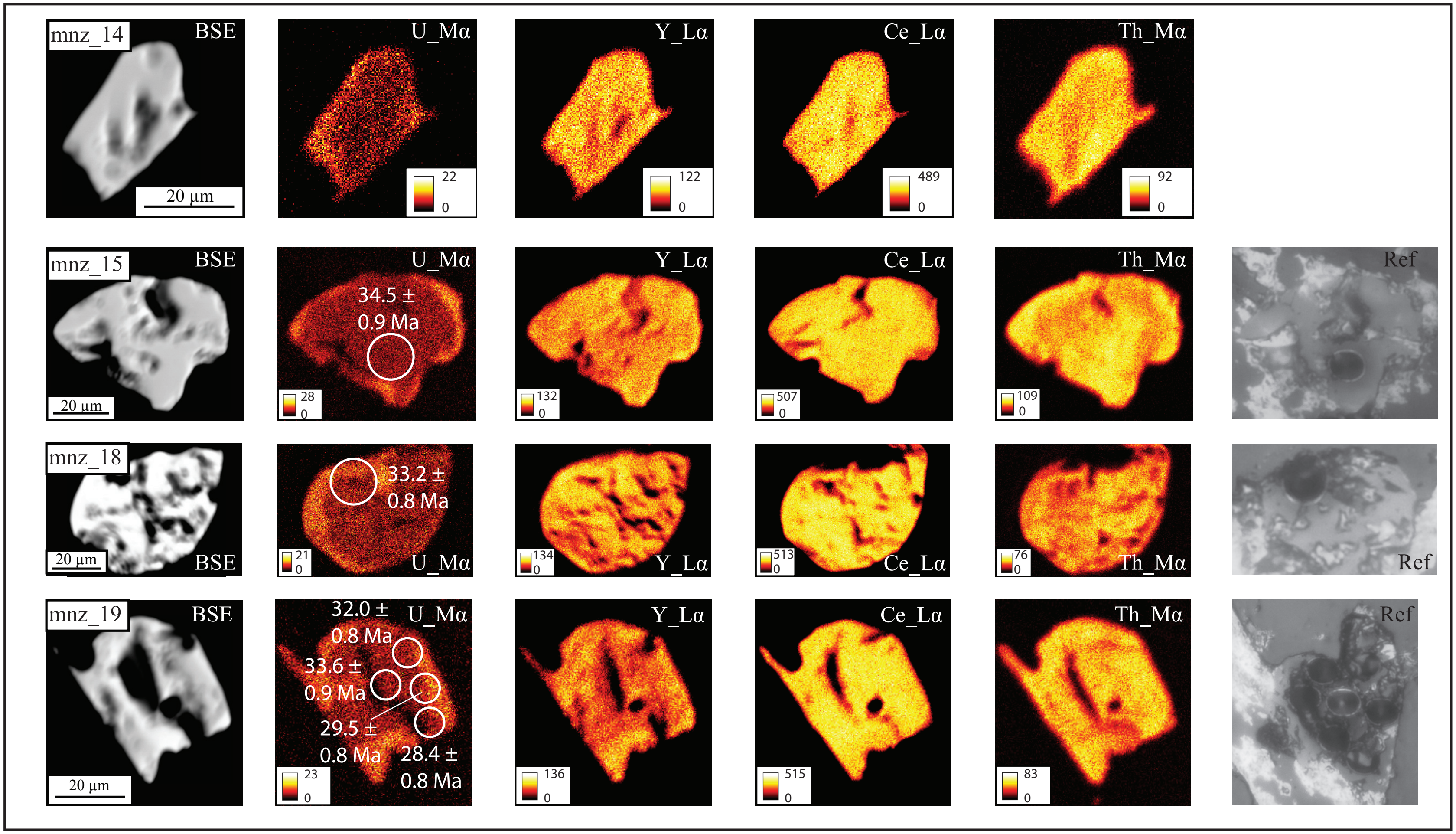

Figure 2A (*continued*).

Table 3A: Monazite isotopic data.

Table 3A.

		Pb	U	Y	Uncorrected isotopic ratios				Uncorrected ages (Ma)		Location[a]
Grain	spot	ppm	ppm	ppm	$^{206}Pb/^{238}U$	1σ %	$^{208}Pb/^{232}Th$	1σ %	$^{208}Pb/^{232}Th$	2σ abs.	
LP13-14											
1	1	94	3162	13040	0.0049	1.9	0.0015	2.3	30.3	0.7	st
1	2	94	3029	12320	0.0049	2.0	0.0015	2.3	30.3	0.7	st
5	1	49	3662	8390	0.0036	2.6	0.0014	3.0	27.6	0.8	ky
5	2	52	1755	7300	0.0047	2.6	0.0016	2.9	32.5	0.9	ky
18	1	72	3650	10810	0.0045	2.2	0.0014	2.4	29.0	0.7	ky
18	2	96	4140	12460	0.0049	2.1	0.0015	2.5	30.7	0.8	ky
18	3	64	3310	10000	0.0048	2.1	0.0016	2.4	31.4	0.8	ky
20	1	81	3790	10920	0.0049	2.2	0.0015	2.5	31.0	0.8	ky
20	3	74	3877	11740	0.0048	2.1	0.0015	2.4	30.0	0.7	ky
20	4	70	3705	11400	0.0048	2.0	0.0015	2.4	30.1	0.7	ky
23	2	72	3028	10600	0.0050	2.0	0.0016	2.4	31.4	0.8	mx
23	3	65	2580	9560	0.0050	2.1	0.0016	2.5	31.8	0.8	mx
24	1	74	3150	10630	0.0049	2.1	0.0015	2.5	31.2	0.8	mx
24	2	78	3350	10460	0.0048	2.1	0.0015	2.5	31.0	0.8	mx
24	3	83	3590	10370	0.0046	2.4	0.0015	2.7	29.7	0.8	mx
28	2	101	4200	12950	0.0048	2.1	0.0015	2.3	30.1	0.7	mx
31	2	66	2274	10270	0.0050	2.1	0.0016	2.4	32.4	0.8	mx
31	3	76	2730	11000	0.0048	2.2	0.0015	2.5	31.2	0.8	mx
31	4	69	2201	10700	0.0049	2.0	0.0016	2.4	31.9	0.8	mx
31	5	79	2340	10560	0.0048	2.0	0.0016	2.5	32.0	0.8	mx
32	1	114	3065	12360	0.0048	1.9	0.0015	2.3	30.8	0.7	mx
32	2	96	2966	11210	0.0048	2.0	0.0015	2.3	31.2	0.7	mx

Table 3A (*continued*).

Grain	spot	Pb ppm	U ppm	Y ppm	Uncorrected isotopic ratios $^{206}Pb/^{238}U$	1σ %	$^{208}Pb/^{232}Th$	1σ %	Uncorrected ages (Ma) $^{208}Pb/^{232}Th$	2σ abs.	Location[a]
LP13-14 (continued)											
32	3	84	4942	12110	0.0039	2.1	0.0014	2.4	27.8	0.7	mx
33	2	79	3456	11950	0.0048	2.0	0.0015	2.4	30.8	0.7	mx
33	3	92	3501	12720	0.0049	2.0	0.0016	2.4	31.6	0.7	mx
33	4	80	3436	12400	0.0049	2.0	0.0016	2.3	31.8	0.7	mx
34	1	74	2963	12010	0.0048	2.1	0.0016	2.5	32.0	0.8	mx
34	2	60	2428	10560	0.0048	2.0	0.0016	2.3	32.2	0.7	mx
34	3	71	3021	11740	0.0049	2.0	0.0016	2.4	32.0	0.8	mx
34	4	65	2916	10050	0.0048	2.0	0.0016	2.4	32.1	0.8	mx
34	5	54	3640	10030	0.0038	2.3	0.0014	2.6	28.3	0.7	mx
37	1	101	2830	11410	0.0049	2.1	0.0015	2.4	30.3	0.7	mx
37	2	108	2699	11920	0.0048	1.9	0.0015	2.3	29.3	0.7	mx
LP09-11											
1	1	90	4700	203	0.0057	2.0	0.0017	2.4	35.0	0.9	og
1	2	88	3609	173	0.0054	2.1	0.0017	2.4	34.4	0.8	og
1	3	66	3836	116.6	0.0052	2.0	0.0016	2.3	33.3	0.8	og
1	4	73	3731	159	0.0053	2.2	0.0017	2.5	34.7	0.9	og
1	5	64	4650	62.5	0.0051	2.0	0.0016	2.4	33.3	0.8	og
1	6	67	4542	32.1	0.0050	1.9	0.0016	2.4	32.9	0.8	og
1	7	76	4067	166	0.0054	1.9	0.0017	2.3	34.5	0.8	og
7	1	79	5948	55.9	0.0048	2.1	0.0016	2.4	31.9	0.8	mx
7	2	67	6570	46.5	0.0046	2.2	0.0016	2.5	32.0	0.8	mx
10	1	56	6390	72.6	0.0041	2.0	0.0015	2.4	30.4	0.7	mx
11	1	95	5055	99	0.0049	2.4	0.0017	2.6	33.4	0.9	mx

Table 3A (*continued*).

		Pb	U	Y	Uncorrected isotopic ratios				Uncorrected ages (Ma)		Location[a]
Grain	spot	ppm	ppm	ppm	$^{206}Pb/^{238}U$	1σ %	$^{208}Pb/^{232}Th$	1σ %	$^{208}Pb/^{232}Th$	2σ abs.	
LP09-11(continued)											
15	1	130	4116	207	0.0052	2.1	0.0017	2.4	34.5	0.8	st
18	1	62	5180	103.2	0.0050	2.0	0.0016	2.3	33.2	0.8	mx
19	1	52	7130	124	0.0038	2.2	0.0014	2.7	28.4	0.8	og
19	2	56	4610	135	0.0041	2.4	0.0015	2.6	29.5	0.8	og
19	3	79	2920	54.9	0.0053	2.4	0.0017	2.6	33.6	0.9	og
19	4	92	4200	56.6	0.0050	2.2	0.0016	2.5	32.0	0.8	og

[a]ky: inclusion in kyanite; mx: matrix; og: inclusion in cordierite overgrowth; st: inclusion in staurolite.

Vita

Kyle White was born in Fresno, CA. He graduated with a B.S. in Geological Sciences from the University of California, Santa Barbara in 2011.